3D CELL CULTURES FOR DEVELOPING MULTIMODALITY DIAGNOSTIC IMAGING TECHNIQUES

BY

CAROL LOUISE SHAFFER

B.S., The Ohio State University, 2004

THESIS

Submitted in partial fulfillment of the requirements
for the degree of Master of Science in Bioengineering
in the Graduate College of the
University of Illinois at Urbana-Champaign, 2007

Urbana, Illinois

Abstract

Three dimensional (3D) cell culture gels are invaluable tools for isolating complex molecular processes associated with cancer. 3D gels were developed for studying multimodality diagnostic imaging of structural and functional features of cancer. The project involves EHS extracellular matrix extract (Matrigel, BD Biosciences) for viewing fibroblast cell proliferation and metabolic activities in a controlled and well characterized microenvironment. These gels were studied by combining mechanical, optical, and magnetic resonance spectroscopic imaging (MRSI) techniques to describe structure (mechanical), cell distribution and phenotype (optical), and metabolic effects (pH imaging via MRSI). After 4 days of culture in the 3D gel, a 5-fold increase in fibroblast number was observed with cell retrieval techniques. Optical coherence tomography (OCT) confirmed proliferative behavior. Using imidazole as an exogenous pH indicator, MRSI showed the cell proliferation reduced gel pH by 0.2. A concomitant increase in collagen production stiffened the gel; the elastic modulus increased 219 Pa. The observed non-uniform cell migration patterns, observed with OCT, provided information regarding cell location and migratory behavior in the gels. The combination of MRSI, mechanical measurement, and OCT can describe essential functional and structural properties. The combination of these imaging techniques will allow future studies of the effects of heterotypic cell signaling essential in tumor development. Because they create known cellular microenvironments characteristic of molecular disease, 3D gels form "living phantoms" for development of detailed multimodality imaging techniques for the study of cancer.

To my friends and family who supported me throughout my education.

Acknowledgments

This project would not have been possible without the support and guidance of many people. Many thanks to my adviser, Michael Insana, for leading the way and supporting the work. Thanks to my MR project team, Diego Hernando, John Stastny, and Justin Haldar, for all their time and hard work determining how to obtain MRSI spectra for my samples, helping me get the setup right, and helping to analyze the data. Thank you to Suresh Kalyanam for all the work on determining correct mechanical indentation measurement. Thank you to Eric Chaney and Sheeny Lan for advice and support with all things cell related. Thank you to Xing Liang for operating the optical coherence tomography equipment. Thanks to the University of Illinois for awarding me with a Support for Under-Represented Groups in Engineering Fellowship and to the National Science Foundation for awarding me a Graduate Fellowship, providing me with the financial means to complete this project. Finally, thanks to my husband, parents, and friends who have been patient and supportive.

Table of Contents

List of Figures

List of Abbreviations

DMEM	Dulbecco's Modified Eagle's Medium
FBS	Fetal Bovine Serum
EHS	Engelbreth-Holm-Swarm
GFP	Green Fluorescent Protein
EDTA	Ethylenediamine Tetraacetic Acid
MR	Magnetic Resonance
MRSI	Magnetic Resonance Spectroscopic Imaging
TE	Echo Time
fid	Free Induction Decay
SNR	Signal to Noise Ratio
SEM	Scanning Electron Microscopy
SVD	Singular Value Decomposition
HSVD	Hankel Singular Value Decomposition
OCT	Optical Coherence Tomography

Chapter 1

Introduction

Multimodality imaging allows multiple aspects of disease, such as structure and function, to be mapped together to improve localization of disease abnormalities. The information of structure and function together clarify the nature of the disease and allow for a more specific diagnosis. Multimodality imaging has peaked interest of physicians in the clinical setting. Traditionally, computed tomography (CT) and magnetic resonance (MR) are used for imaging anatomical changes, while molecular imaging techniques, such as positron emission tomography (PET) and single photon emission computed tomography (SPECT), are used to show functional or metabolic changes of pathology [38]. Combining these techniques in multimodality imaging provides a clinician with a greater understanding of the disease state with anatomical information and also the underlying functional cause. Much research has been done with combinations of SPECT and CT, PET and CT, and PET and MR.

The use of anatomic and functional image fusion is increasing in nuclear medicine, especially in oncology. For example, the clinical usefulness of ^{131}I SPECT/CT fusion imaging was demonstrated Yamamoto, et al. on patients with differentiated thyroid carcinoma [42]. ^{131}I SPECT is used to localize thyroid tumors by visualization of ^{131}I uptake. However, without anatomical markers, precise localization is difficult [42]. Yamamoto et al. fused ^{131}I SPECT and CT images using external markers placed at specific positions on the patient's body and matching images using a fusion algorithm based on a point-match method. It was shown that with the addition of anatomical information from CT, ^{131}I SPECT image interpretation and precise tumor localization can be improved. The accuracy of matching the external markers was sufficient, but this error would be eliminated by combined CT/SPECT scanners that allow the patient to be scanned in a single position. However, combined scanners are high in cost and are not readily available [42].

Indispensable medical imaging techniques, such as PET, have been useful in quantification of biochemical processes. However, PET presents some drawbacks, such as limited spatial resolution (4-6mm for most systems) and underestimation of activity in small structures that allows these regions to be missed [18]. With the addition of MR images co-registered with PET images, anatomic localization of lesions and quantification of tumor uptake in smaller lesions subject to partial volume effects can be improved [18]. The combination

of MR and PET information could improve a clinician's accuracy in determining the condition during early phases of disease progression.

Most multimodality imaging research and clinical applications have focused on combining techniques for use at the full body and tissue level. The development of imaging modalities at the cellular level to study and define disease states is an essential first step before future large scale build up into full tissue imaging. In diseases, such as cancer, it is integral to image at cellular levels and improve spatial resolution at this scale in order to improve diagnosis and treatment. For example, cancer treatments are less successful in heterogeneous solid tumors where hypoxic regions of low blood flow fail to respond fully to the treatment. Safe and low-cost imaging techniques able to detect regional acidic and hypoxic conditions during treatment could significantly improve patient outcome [22] [11]. High spatial resolution is important to localize these acidic environments.

Three dimensional (3D) cell culture tissue models offer the exciting possibility for developing new diagnostic imaging modalities at the cellular level with improved diagnosis specificity because they can mimic the physiological microenvironment of intact tumors in a controllable and well characterized manner. Cell cultures serve as invaluable tools for investigations into complex molecular processes within and among cells of cancerous tumors. Molecular processes associated with cancer can be isolated and studied. A multimodality approach to studying the culture allows different types of functional and structural information to be obtained and analyzed simultaneously regarding these processes. The culture serves as a "living phantom" and can also be used to cross-validate the information gained with each imaging modality.

Carcinoma development is a complicated process that begins as a mixture of a variety of cell types, such as fibroblasts, endothelial cells, smooth muscle cells and inflammatory cells [11]. The epithelial tumor cells interact with the basement membrane and stromal cells (adipocytes, fibroblasts, endothelium). The stroma is usually made mostly of fibroblast cells, but this varie in different organ systems [11]. The stroma is responsible for the desmoplastic response, or stiffness effect, in malignanat tumor development, which is characterized by increased extracellular matrix proteins; e.g., collagens, fibronectin, proeoglycans and glycosaminoglycans. Myofibroblasts, a specific type of fibroblast with increased proliferative characteristics for extracellular matrix proteins, are primarily responsible for the stromal response because of their high amounts of collagen secretion and ability to contract tissue [11].

Another well-known characteristic of cancerous tumors is increased acidity in the extracellular space called acidosis. This acidity has been attributed to altered glucose metabolism and increased glucose uptake. The increased glucose metabolism has been correlated to increasing tumor aggressiveness and invasive characteristics [16]. Tumor cells adapt, survive and proliferate in this acidic environment, while normal cells

cannot and die via apoptosis. The space that the dead cells leave is then invaded by proliferating tumor cells [16]. This acidic characteristic of tumor invasion offers an opportunity to develop and improve imaging techniques that target the detection of this environment for improved diagnosis.

The above description of cancerous tumor characteristics and mechanisms of development are complex and not yet well understood. Interactions between epithelial cells and the stroma in tumor progression involve interactions with multiple cell types, growth factors, extracellular matrix proteins, proteases and protease inhibitors in different stages such as desmoplasia, angiogenesis, invasion and metastasis [11]. It is essential that scientists and medical researchers start with studies to gain understanding of the most simple of these cellular processes and build to more intricate cell signalling and behaviors.

To study processes involved in cancerous tumor formation, imaging techniques can be developed and used in tandem to observe structure and function of a well characterized model. In this project, a three dimensional tissue culture was developed and used to design a multimodality imaging approach to obtain biochemical and mechanical information as well as track cell movement within the culture.

Multiple modalities were used to examine changes in pH and mechanical properties of a three dimensional fibroblast culture temporally, while also following proliferation and motion of the cells within the volume. Three dimensional cultures were designed using matrigel basement membrane matrix seeded with fibroblasts cells. Fibroblast behavior in vivo and in cell culture has been well characterized previously. Therefore, these cells are ideal for the initial development of the imaging techniques and experimental designs. The physical properties of matrigel have not been well characterized regarding effects of temperature and CO_2 concentrations in the air on pH. Therefore, initial studies of the material itself were conducted. The goals of the project were as follows:

- Characterize matrigel material for experimental design and setup.
- Quantify fibroblast proliferation in matrigel.
- Develop a magnetic resonance spectroscopic imaging (MRSI) technique to study metabolic changes via spatial mapping of pH in 3D culture.
- Develop an indentation technique to measure mechanical changes of the 3D culture.
- Use optical coherence tomography (OCT) to locate fibroblasts within the matrigel.

The combination of modalities and studies described offer a unique set of data that allows determination of fibroblast biochemical, structural and migratory behaviors spatially and with culture time in the matrigel. Most importantly, the establishment of these techniques and culture geometries offer the opportunity to study advanced cultures of biologically relevant cancer environments.

Chapter 2

Methods

2.1 Cell Culture

NIH 3T3 Mouse Embryonic Fibroblasts were cultured in $T-75$ flasks using DMEM media supplemented with 10% fetal bovine serum (FBS). The cultures were maintained in a 37°C incubator with 5% CO_2 in air. For matrigel sample preparation, media was removed and cells were lifted from the flask surface using first, a 4ml phosphate buffered saline wash, followed by incubation for 5 minutes in 3ml of trypsin. 6ml of media was added to the cell suspension and then the solution was centrifuged for 5 minutes at 1000 RPM. The supernatant was removed leaving the cell pellet. The cells were re-suspended in an appropriate volume of media (between $4-6$ml depending on cell number estimation). 40μl of the solution were mixed with 40μl of trypan blue to stain the dead cells. 9μl of the trypan blue/cell mixture were added to each side of a hemacytometer and the live and dead cells were counted. A portion of the NIH 3T3 cells were transfected with a green fluorescent protein (GFP)-vinculin plasmid by Dr. Stephen Boppart's laboratory as described previously [37]. These cells were maintained in the same manner as the other NIH 3T3 cells.

2.2 Three Dimensional Matrigel Sample Preparation

Matrigel (BD Biosciences, Franklin Lakes, NJ) was seeded with fibroblast cells at a density of $100,000$ cells/ml matrigel. Before sample preparation, the matrigel was kept in 4°C in a sterile vacuum for at least 48 hours to remove dissolved gasses. For samples used in mechanical, cell density, OCT, and collagen staining studies, cell solutions of 25μl media containing $100,000$ were placed in a 15ml centrifuge tube. 1ml of matrigel was added at 4°C to the cell solution using a pre-cooled pipette. The matrigel and cells were mixed completely, avoiding the introduction of air. The mixture was then added to a 12-well plate cell culture insert with diameter of 12mm (Millipore 12 well plate cell culture insert with hanging geometry and 1μm transparent polyethylene terephthalate bottom membrane). The solution was placed in a 37°C incubator with 5% CO_2 in air for 30 minutes to gel. The resulting gel was approximately 7mm in height. 1ml of media

was then added on top of the gel, and it was placed back into the incubator until experimentation. For 6 day studies, sample media was changed daily. For samples used in the MRS studies, 50mM of imidazole was added to the matrigel before refrigeration in a vacuum for 48 hours. The matrigel solution was seeded with $100,000$ cells/ml of matrigel as previously described. Each sample was 2ml in volume and was contained in a 12mm x 75mm borosilicate test tube. The resulting gel was approximately 22mm in height. After the initial 30 minute gel period in the incubator, 2ml of media was added on top of the gel. For 5 day studies, the media was changed daily on the samples. A flow diagram for sample preparation is shown in Figure 2.1

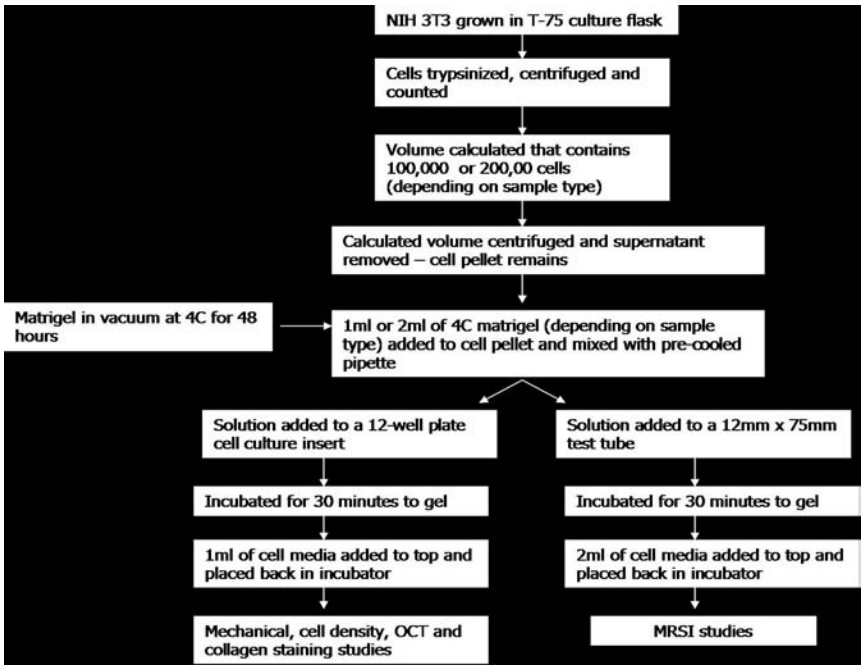

Figure 2.1: Matrigel Sample Preparation Flow Diagram

2.3 Imaging of GFP-vinculin Labelled Fibroblasts in 2D and 3D Culture

Much research has been done to show the benefits of 3D in vitro culture, as opposed to 2D culture. Three dimensional culture provides a more natural environment for cells to proliferate and metabolize as they would in vivo. To successfully investigate cell behavior, it is necessary to recreate the three-dimensional architecture of the natural tissue [24]. This is largely due to the importance of architectural cues to which cells respond [24]. Images of GFP-vinculin labelled fibroblasts were acquired in both 2D and 3D cultures.

The structural differences among the cells in these cultures is evident via microscopy.

GFP-vinculin labelled fibroblasts were imaged on the bottom of a T-75 flask (Figures 2.2 and 2.3). Fluorescence was detected using a Q-COLOR 3 cooled CCD, an IX51 inverted microscope, and QCapture Pro software (all Olympus). An FITC emission/excitation filter for 488nm was used to capture the fluorescence of the GFP.

Vinculin is an abundant cytoskeletal protein found in integrin-mediated focal adhesions and cadherin-mediated cell-cell adheren junctions [37]. In the images, the vinculin glows green as a result of the GFP label. It is evident that the fibroblasts are adhering to both the surface of the flask and to each other in these images. The cell bodies appear stretched out with thin reaching projections.

GFP-labelled fibroblasts were also imaged in three dimensional matrigel using confocal microscopy. Confocal microscopy permits optical sectioning of a fluorescent sample. It uses a pinhole to reject light coming from outside of the focus area. The confocal microscope used was a Leica Microssystems model TCS SP2 RBB. An argon laser line of 488nm to excite the GFP labelling. Resolution in the xy directions is 650.7nm and in the z direction, 4767.6nm.

As can be seen in Figure 2.4, the cells in the three dimensional matrigel environment appear round, unlike the stretchy behavior in 2D culture. However, the detection of the GFP means that they are again adhering to their environment, which in this case is the gel. It has been shown in prior study that non-malignant cells appear round in matrigel and grow in colonies, while malignant cells form large cellular extensions [25].

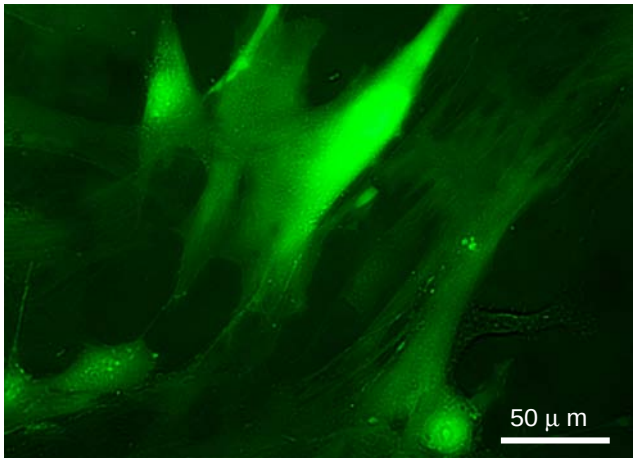

(a)

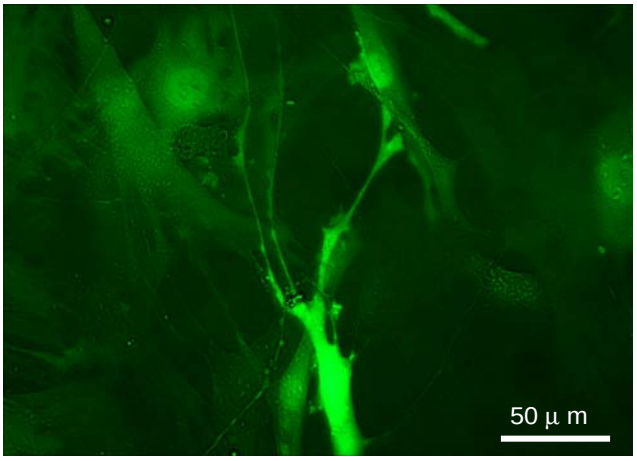

(b)

Figure 2.2: GFP Labelled Fibroblasts on Plastic Surface of Flask

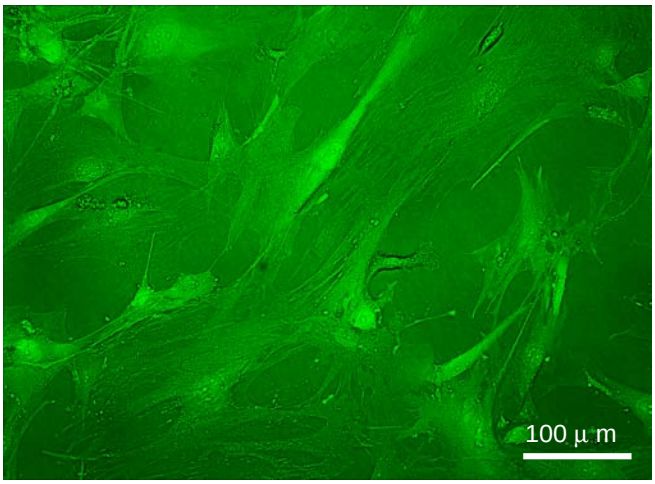

(a)

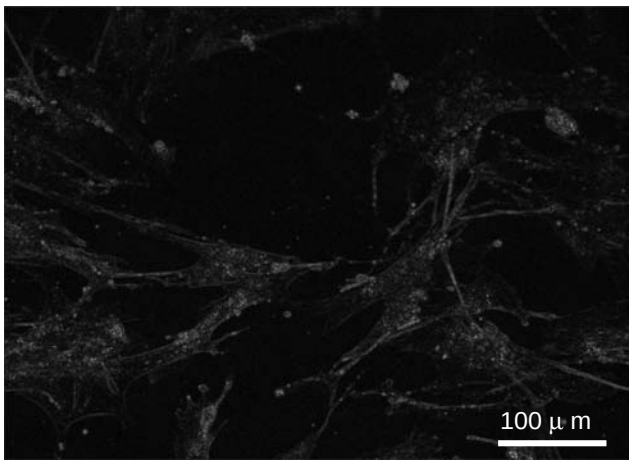

(b)

Figure 2.3: Fibroblasts on Plastic Surface of Flask; (a) GFP Labelled Fibroblasts; (b) Black and White Photo of Fibroblasts

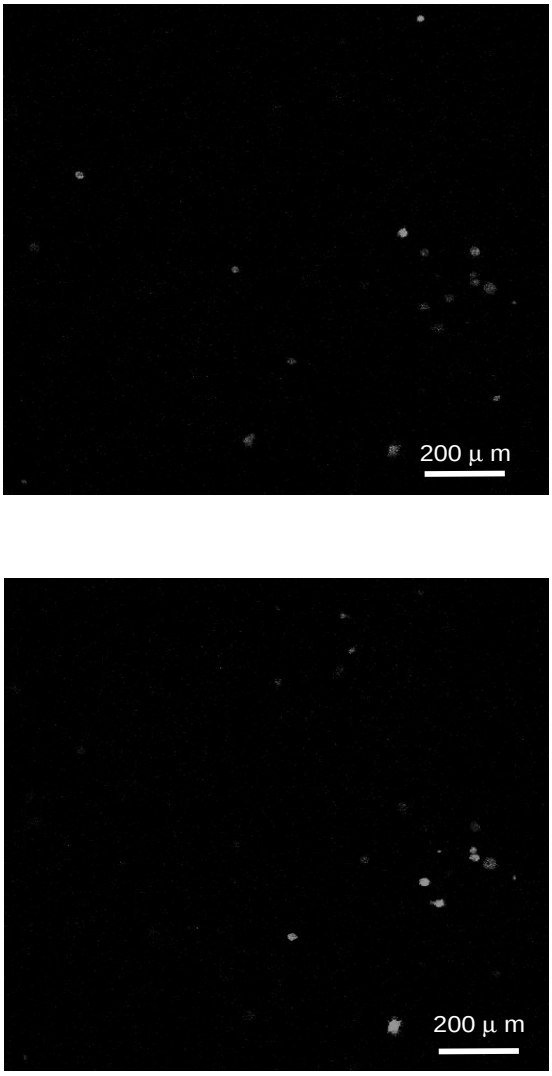

Figure 2.4: Confocal Microscopy Images of GFP-labelled Fibroblasts in 3D Matrigel Culture

2.4 Scanning Electron Microscopy Imaging of Matrigel

Images of matrigel, without cells, were taken using an XL30 ESEM-FEG environmental scanning electron microscope (FEI Company, Hillsboro, OR) in HiVac mode at 5 kV and a spot size of 3 (2.1 nm). These images show the detailed structure of the matrigel material.

The matrigel was kept overnight in 2.0% paraformaldehyde and 2.5% glutaraldehyde in 0.1M Na-Cacodylate buffer with pH 7.4. The sample was rinsed with 0.1 M Na-Cacodylate buffer for 10 minutes. For post-fixation, the sample was placed in 1.0% aqueous osmium tetroxide in 0.1M Na-Cacodylate buffer in a dark hood for 90 minutes. The sample was again rinsed for 10 minutes with 0.1M Na-Cacodylate buffer. For dehydration, the sample was placed in 37%, 67%, and 95% ethanol solutions in succession for 10 minutes each. It was placed in 100% ethanol three times for 10 minutes each. The sample was then dried in a critical point drier. The sample was broken into pieces to view fracture surfaces in the scanning electron microscope (SEM). These images are shown in Figure 2.5.

The images show that the matrigel has pores between approximately 100nm and 700nm in diameter. In a previous research study, also using SEM, the matrigel sample was found to have pore sizes averaging 105nm $\pm$ 70nm with a range of 26-359nm [1]. The pore sizes deduced from Figure 2.5 are on the same scale as those published previously. The matrigel pores have fibrous networks throughout. This structure is a random network of loosely knit fibers forming the pores. The pores allow cells to move throughout the matrix and remodel as necessary. The porous structure also allows media to seep into the gel to provide nutrients to the cells.

2.5 Measurement of Matrigel pH with Temperature and 5% CO_2

In order to design experiments involving matrigel, the material properties for the gel itself were necessary to investigate. Matrigel contains a bi-carbonate buffer that reacts with CO_2 in the air. According to the manufacturer, BD Biosciences, it is designed to stabilize the pH at a value around 7.4 in an incubator environment of $5\%CO_2$ and 37°C. Investigation was necessary to discover if/how the pH would change in other environments. For pH and mechanical experimentation, successful measurements depended on keeping properties of the gel consistent. A change in pH with a change in temperature or $\%CO_2$ could change the chemical properties of the gel and bias the results of the MRSI pH study.

pH was measured within the media placed on top of the matrigel sample using a micro glass-body liquid filled combination electrode (Denver Instruments, CO). Like matrigel, the cell media has a bi-carbonate buffer system, and it is assumed that the media and matrigel maintain equilibrium with each other in

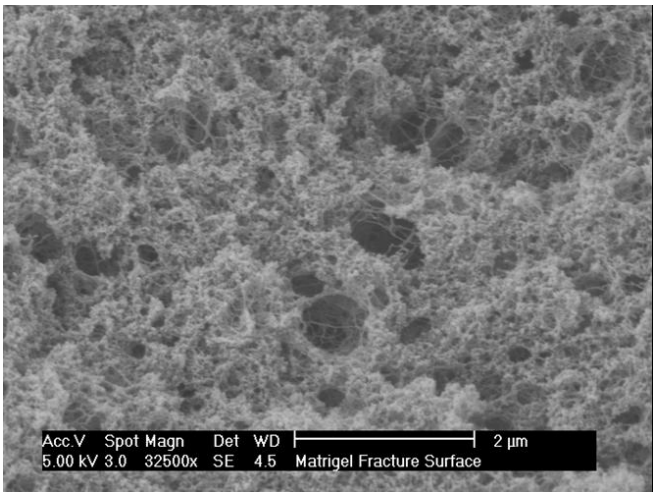

(a)

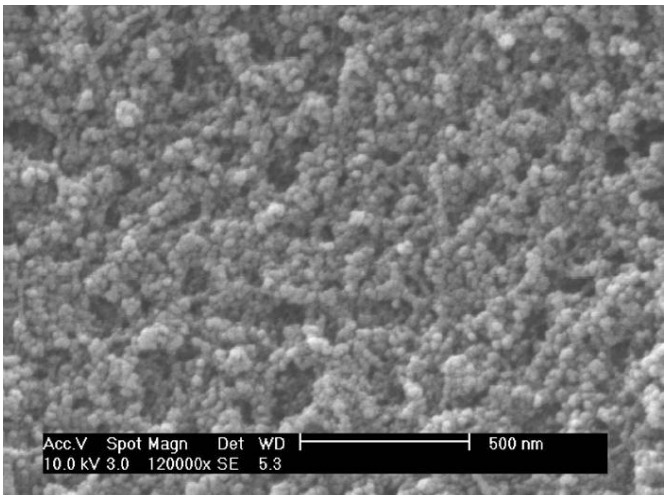

(b)

Figure 2.5: SEM Images of Matrigel

regards to pH. This assumption is justified when considering matrigel's porous structure when gelled (See Figure 2.5). Therefore, measurement of pH in the media is assumed to indicate pH of the matrigel.

Matrigel samples for the pH study were prepared similarly to those described in the previous section. However, fibroblasts were not added to the matrigel. Matrigel was introduced into the 12-well plate cell culture inserts as a liquid at 4°C. After the 30 minute gelation in the incubator, 500μl of culture media (DMEM with 10%FBS) was added to the top of the sample. The sample was placed back into the incubator for 30 minutes for equilibration with the 5% CO_2 environment. Next, a pH probe was inserted into the

media while the sample was inside of the incubator. Then, pH was recorded from outside of the incubator for the next 10 minutes, once every minute. From this point, the sample was taken to one of four test environments and pH was recorded every minute for 2 hours. The four environments were as follows: 27°C with 5% CO_2, 37°C with 5% CO_2, 37°C with normal room air, and room temperature (23°C) with room air. The results are shown in Figure 2.6.

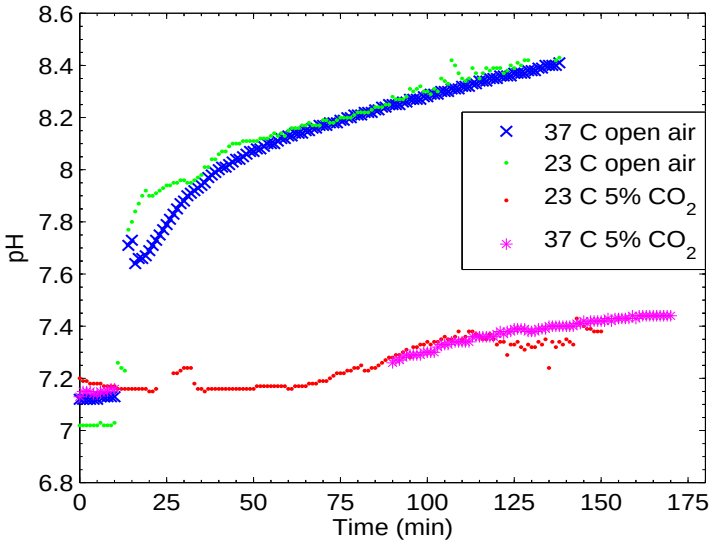

Figure 2.6: Matrigel pH with Time and Temperature

The study showed that the pH went up significantly to approximately 8.4 in open air at both 37°C and 23°C. At both 37°C and 23°, with a 5%CO_2 air concentration, the pH started at about 7.15 and slowly increased to approximately 7.4. It took almost the entire length of the study for the pH of 7.4 to be reached in 5%CO_2. Nevertheless, the results of this pH study of matrigel show that the pH of the gel increases as the CO_2 concentration decreases. However, the air temperature did not affect the pH. Therefore, for the MRSI study, the CO_2 was controlled to 5% inside the sample container. Similarly, for the mechanical study, air containing 5%CO_2 flowed over the sample during experimentation.

2.6 Cell Density Determination

Eighteen samples (3 samples for each day of a 6 day study beginning with day 0) were prepared with 100,000 cells/ml of matrigel. Samples were placed in 12-well plate cell culture inserts as described in the previous matrigel sample preparation section. Each day, the cell within three gel samples were recovered for counting. The medium was removed from the sample and 1ml of dispase (BD Biosciences, Franklin Lakes, NJ) was

added. The sample was returned to the incubator for 3 hours to allow complete dissolution of the gel. Next, the sample was removed from the incubator and the dispase/cell/matrigel was mixed with a pipette in the insert before removing the liquid suspension and placing it in a 15ml centrifuge tube. 1ml of 5mM EDTA solution was then added to the empty cell insert and mixed in and out with a pipette to obtain any cells that may have remained on the insert. The EDTA was then added to the cell suspension in the 15ml centrifuge tube and mixed thoroughly to stop the action of the dispase. The sample was then centrifuged at 1000 RPM for 10 minutes. The supernatant was removed leaving the pellet of cells behind. 500μl of media was added to the pellet and mixed well. The cells in the solution were then counted using a hemacytometer.

The efficiency of retrieving cells from the gel was calculated on day 0 as number of cells counted divided by the 100,000 cells originally introduced into the gel. This efficiency factor, which was determined to be 0.56, served as a correction factor for all samples as it can be assumed that the efficiency of retrieving cells from the gel remained constant. In the samples for days 1, 2, 3, 4 and 5, 1ml of media was changed each day. A flow chart diagram for cell retrieval from the gel is shown in Figure 2.7.

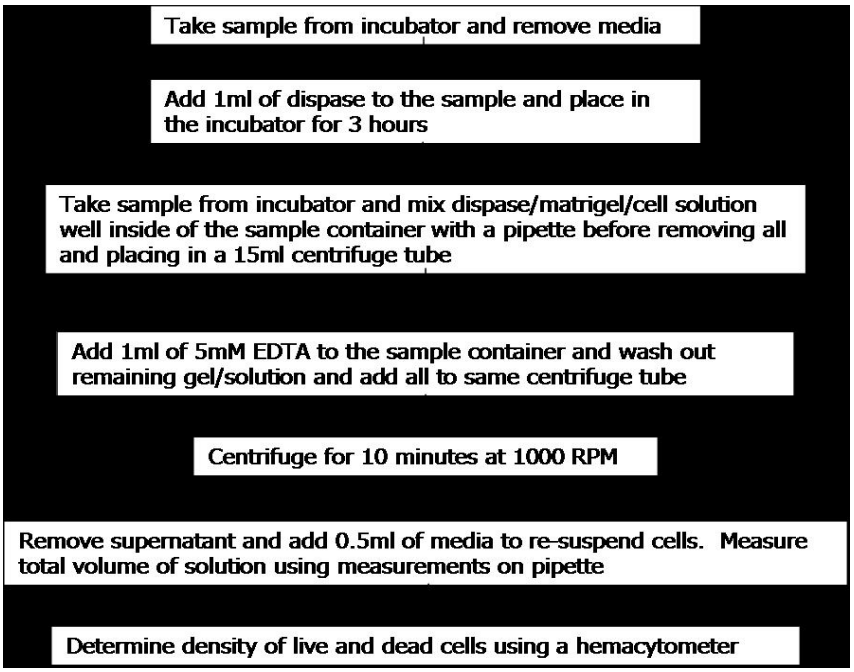

Figure 2.7: Cell Density Cell Retrieval Flow Diagram

2.7 MRSI Measurements of pH

Tumors frequently exhibit areas of hypoxia and a build-up of lactate, extracellular acids, and other metabolites. MRSI of nuclei such as ^{31}P, ^{13}C can be used to measure concentrations of metabolites in tumors [17]. ^{13}C has been used for studying metabolic fluxes and intermediary metabolism. Glucose can be labelled with ^{13}C to determine the glycolytic rate of a tumor [17]. ^{31}P has been used to detect metabolites and can resolve signals from phosphomonoesters and phosphodiesters in vivo. It was used to show that the phosphomonoesters signal decreased in breast tumors responding to chemotherapy [17]. ^{31}P chemical shift imaging provides an estimate of pH, a metabolic marker, using the pH-dependent chemical shift between P_i and an endogenous reference such as phosphocreatine or alpha nucleoside triphosphates [17].

Although useful information regarding metabolism can be obtained using MRSI of ^{13}C and ^{31}P, abundance of these ions is low. As an alternative, ^{1}H has been shown to be a more MR sensitive nuclei and ^{1}H-based MRSI allows superior spatial resolution of spectral data. Spatial localization of the metabolites is more easily obtained [17]. ^{1}H-based MRSI can be used to obtained pH estimations and generate pH spatial maps. However, there are no endogenous markers for ^{1}H, so exogenous indicators must be used. Imidazole has been used as an indicator because it has a spectral resonance far enough from endogenous signals to be easily distinguished [15].

2.7.1 Imidazole Indicator

Imidazole has been used previously as an exogenous ^{1}H NMR pH indicator, most notably for pH measurement inside red blood cells [34]. Protons attached to the imidazole carbon ring (CH) resonate in a vacant region of the biologically relevant spectrum. The protons attached to the nitrogen (NH) affect the C2-H chemical shifts and have pK_a values between 6 and 9 [15]. The three imidazole ring carbons are labelled 2, 4 and 5 as seen in Figure 2.8.

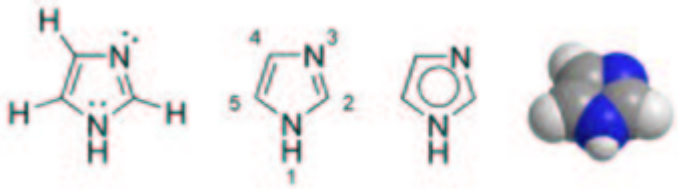

Figure 2.8: Imidazole Chemical Structure Showing Labelling of Carbons

Imidazole was used in this project as an indicator to detect extracellular pH inside of a matrigel sample containing NIH 3T3 Mouse Fibroblasts. The imidazole appears as two peaks in the fid spectrum separated by a distance (in ppm) that can be mapped to a previously determined calibration curve to find the pH value.

The calibration curve was determined through measurement of a solution containing 10mM imidazole, 140mM KCl, 5mM NaH_2PO_4, and 2mM trimethylsilylpropane sulfonic acid. Solution pH was adjusted using 0.1M HCl or KOH. This solution used for obtaining the calibration curve was modified from that previously described by C. Gasparovic [15]. Sixteen pH values between 5.5 and 8.0 were prepared and the chemical shifts were measured.

The calibration data was fit to the Henderson-Hasselbalch equation. In this pH model, an indicator species is assumed to have a pH dependent chemical shift resulting from a rapid equilibrium between acid and conjugate base forms of the indicator species [2]. The Henderson-Hasselbach equation is shown in Equation 2.1.

$$pH = pK_a - \log_{10}\left(\frac{\delta_{obs} - \delta_{acid}}{\delta_{base} - \delta_{obs}}\right) \tag{2.1}$$

δ_{obs} is the MR spectrum chemical shift of the sample in ppm. pK_a is the negative $\log_{10}$ of the acid dissociation constant for the indicator species (Equation. 2.2).

$$pK_a = -\log_{10}(K_a) \tag{2.2}$$

For the calibration curve, rather than using the absolute value of the chemical shift of the left peak, the difference in chemical shift between the two imidazole peaks can be substituted. Call this difference $\Delta\delta_{obs}$ and again consider the Henderson-Hasselbach equation. However, in this case, the observed chemical shift, δ_{obs}, is replaced by the observed chemical shift difference, $\Delta\delta_{obs}$, between the two imidazole peaks. This modified Henderson-Hasselbalch equation is given by:

$$pH = \alpha_1 - \log_{10}(\frac{\Delta\delta_{obs} - \alpha_2}{\alpha_3 - \Delta\delta_{obs}}) \tag{2.3}$$

α_1,α_2 and α_3 are constants found through curve fitting and do not have physical significance.

A non-linear least squares fit was obtained for the calibration data using Matlab's optimization toolbox. The corresponding parameters are:

$$\alpha_1 = 7.24$$

$$\alpha_2 = 1.21$$

$$\alpha_3 = 0.64$$

The root mean square error for the fit was 0.018 ppm or 0.022 pH. The calibration curve is shown in Figure 2.9.

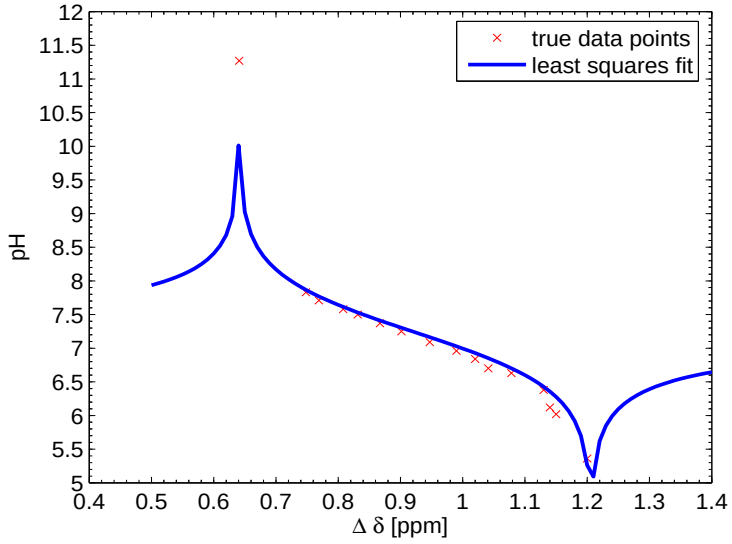

Figure 2.9: Calibration Curve Used for pH Determination in MRSI Study

The distance between the two imidazole peaks was measured in the spectrum as $\Delta\delta$ in units of ppm as shown in Figure 2.10. The pH was then determined from this distance on the calibration curve, which is shown zoomed in on Figure 2.11. This process was used for all pH measurements in control and study samples.

2.7.2 Experimental Setup

The matrigel sample was contained in a 12mm x 75mm test tube as described previously in the sample preparation section. The test tube was placed into a coil in a 14.2 Tesla Varian MR system as shown in Figures 2.12 and 2.13. Air containing 5% CO_2, 10% O_2 and balanced with nitrogen flowed slowly through media for humidification and then into the space above the sample through a stopper. An exhaust tube in the stopper allowed continuous airflow throughout experimentation to obtain spectra of the sample. This environment allowed the pH to remain stable and consistent with the 5% CO_2 incubator environment.

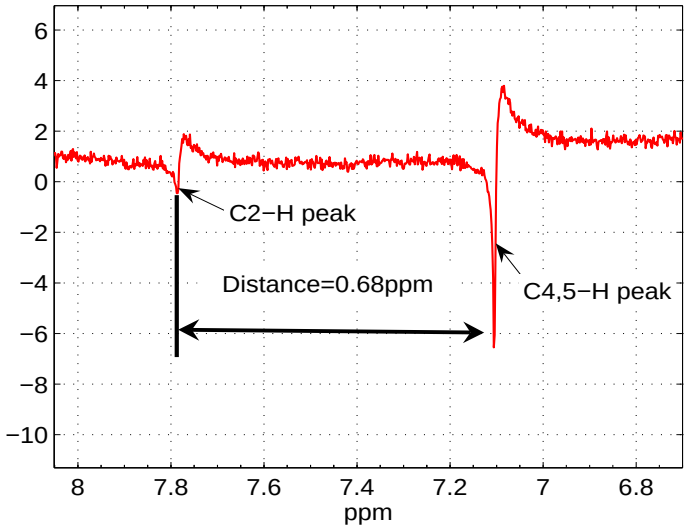

Figure 2.10: Determination of $\Delta\delta$ppm Between Peaks in MRS Spectrum. This value corresponds to a pH value of 8.36.

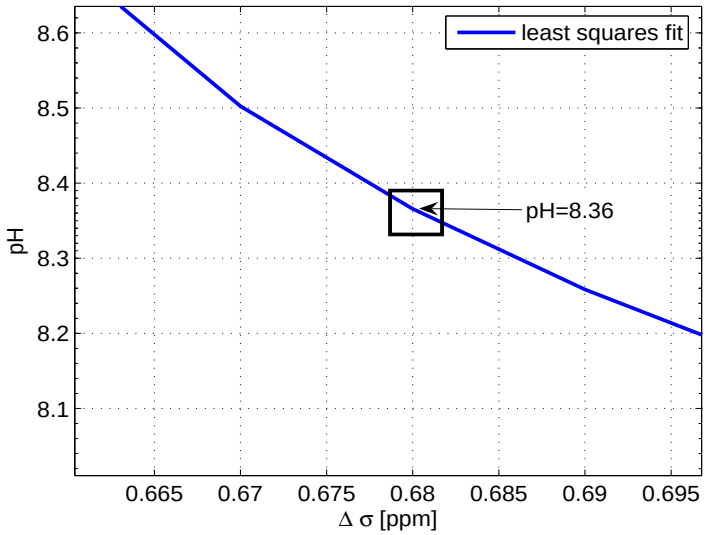

Figure 2.11: Closeup of pH Determination from $\Delta\delta$=0.868ppm (Fig. 2.10)

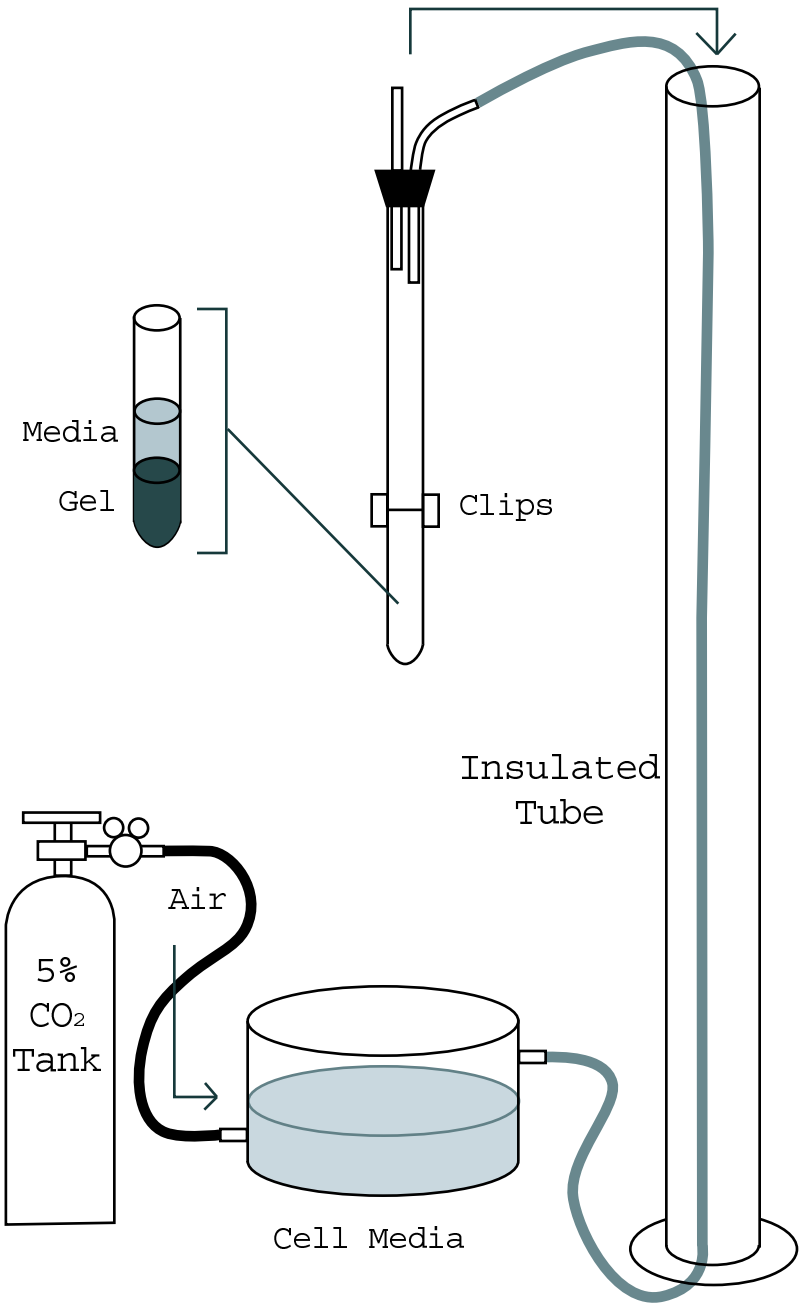

Figure 2.12: MRSI Measurement Experimental Setup: Sample Holder

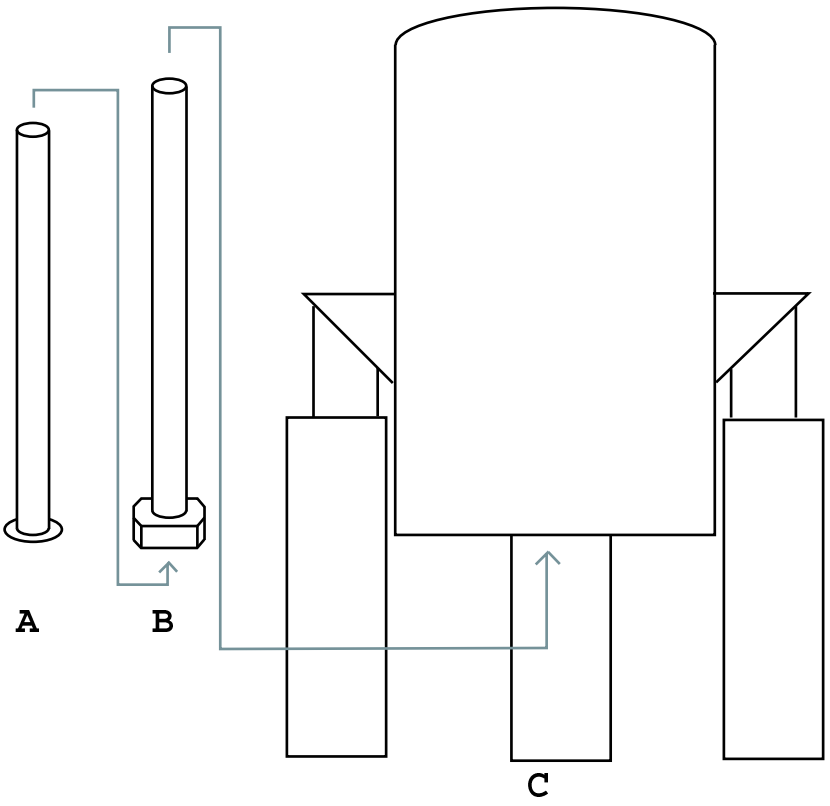

Figure 2.13: MRSI Measurement Experimental Setup: Sample with Magnet Setup

2.8 MRSI Data Acquisition and Processing

2.8.1 MRSI Spectroscopic Imaging Pulse Sequence

A diagram of the MRSI pulse sequence employed is shown in Figure 2.14. This sequence was developed by Justin Haldar, a Ph.D. student at UIUC in Electrical Engineering, and has been modified for this project to allow independent control of the crushing gradient amplitude.

The pulse sequence consists of a hard (non-frequency selective) 90° pulse, followed by refocusing/slice-selection pulses along 3 spatial coordinates. The intersection of the 3 selected slices forms the selected volume (of size $9 \times 4 \times 4$ mm in our case). Refocusing is achieved by using adiabatic RF pulses [8, 35], which are particularly immune to RF field inhomogeneities as well as chemical shift. This technique produces a more accurate refocusing of the imidazole signal, which oscillates with a frequency several *ppm* apart from the

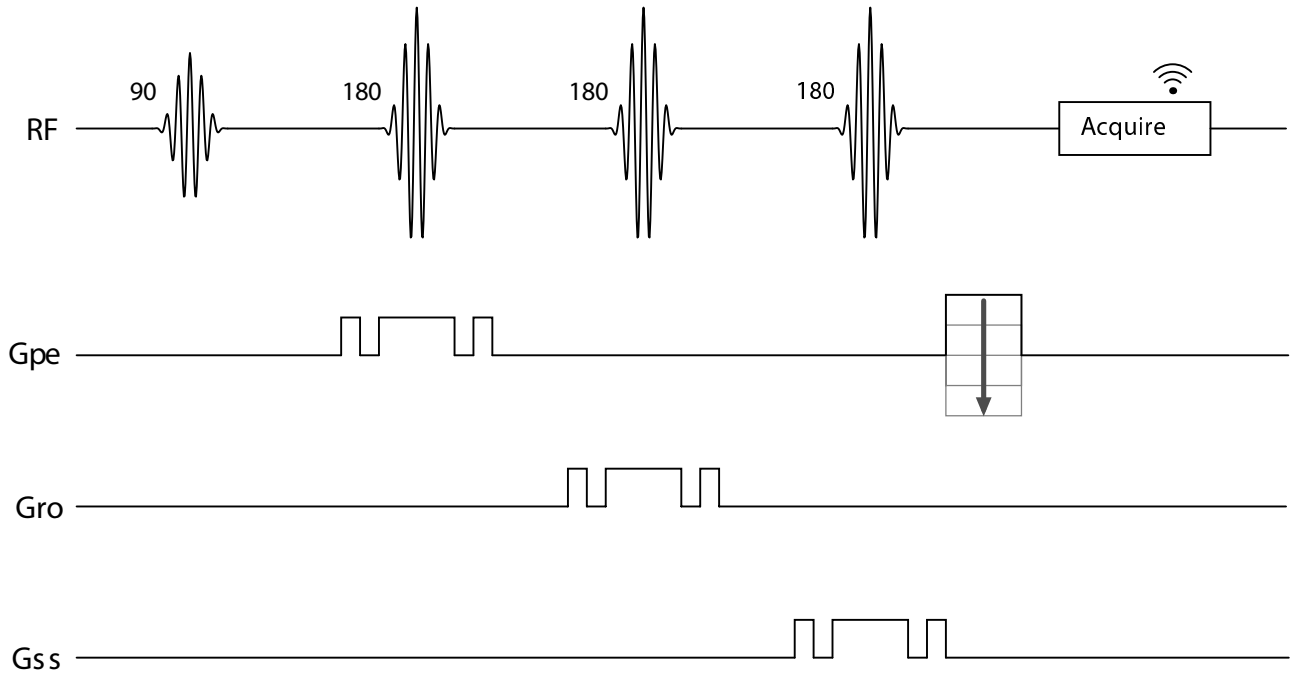

Figure 2.14: View of the MRSI Pulse Sequence

water signal). One disadvantage of adiabatic pulses is that they introduce a nonlinear, position-dependent phase and so must be used in pairs of identical pulses in order for the second pulse to cancel the phase introduced by the first one. Additionally, refocusing pulses produce spurious signals because the flip angle is not exactly 180°. The spurious signals must be eliminated by applying crushing gradients before and after each pulse. Crushing gradients before the pulse de-phase the signal. The second crushing gradient, after the pulse, places the desired signal back in phase and de-phases the spurious signal.

The signal is acquired at the echo time (TE), after application of the phase encoding gradients. Only the *fid* on the right-hand side of the echo is acquired.

Water suppression has not been employed. It is optional within the current sequence, and implements the *CHEmical Shift Selective* (CHESS) method adding 8 additional pulses before the 90° pulse. Thus, water suppression requires considerably longer TE. Instead, water removal is performed during postprocessing of the spectra, as described below.

2.8.2 Choice of Pulse Sequence Parameters

Position and Size of Selected Volume

The selection of the sample volume is shown as a box in the MR image of Figure 2.15. The selected volume is $9 \times 4 \times 4$ mm with the top located $0.5 - 1.0$ mm below the media-gel interface, which is indicated by the

curved line in the figure.

The size of the volume presents a tradeoff between signal to noise ratio (SNR) and field inhomogeneity. On the one hand, larger volumes provide more signal (thus requiring fewer averages), but on the other hand it is easier to obtain a more homogeneous field over smaller volumes. In this case, it is possible to consistently obtain a water peak linewidth (defined as *full-width at half max*) between $3.5 - 7.0$ Hz over our selected volume as long as there are no air bubbles in the vicinity. This linewidth is enough to clearly observe the C4,5-H (rightmost) imidazole peak over the whole volume. The C2-H peak can usually be observed over the whole volume as long as no pH gradient is present.

The position of the volume is chosen as close as possible to the interface without reducing the field homogeneity. It would be ideal to reach the interface with the selected volume, but susceptibility effects make shimming much harder. In this study, the top portion of the data had to be discarded whenever the selected volume was too close to the interface, due to poor shimming. A distance of $0.5 - 1.0$ mm has shown to be a good compromise.

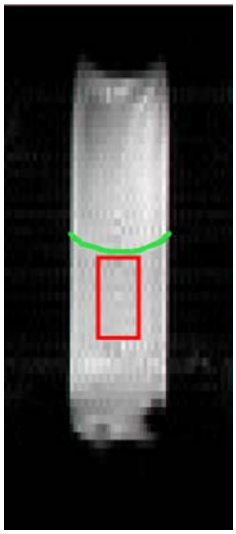

Figure 2.15: Coronal Slice (spin-echo image) and Selected Volume of MRSI Sample

Phase Encodings

The sample is assumed to be homogeneous in the horizontal dimensions. Thus, phase encoding was applied only along the vertical direction to obtain spatial resolution for pH estimates. For a 10 mm in the vertical field of view, 20 phase encodings are applied producing a voxel thickness of 0.5mm. However, leakage occurs between adjacent voxels due to the point spread function of the Fourier reconstruction. In order to achieve minimum acceptable SNR, 256 averages are obtained, resulting in a total scan time of 130 minutes. For

control experiments, only 10 phase encodings are used for a resolution of 1mm, which requires 128 averages and a scan time of 33 minutes.

Echo Time and Crushing Gradients

Due to slight imperfections in the refocusing pulses, spurious signals are created, which need to be removed before the desired signal is acquired. A crushing gradient strength of 9 G/cm is applied for tcrush = 900 μs before and after each refocusing pulse.

Shorter TE produces more signal, but longer TE typically results in a spectra with sharper peaks(since spurious signals usually decay faster than the desired imidazole peaks). In addition, large values of tcrush require longer TE in order to fit all the crushing gradients before the echo time. In this experiment, TE values between 50 ms and 70 ms produce the best results.

Other Parameters

Calibration of the transmit power for the adiabatic RF pulses. Adiabatic pulses are ideal for routine work because calibration of RF power does not need to be particularly accurate [26]. In this case, $51 - 52$dB has shown to work well under the present experimental conditions.

Field of view. The field of view along the vertical direction is chosen slightly larger than the height of the selected volume. In this case, the volume is 9mm high and the field of view is chosen to be 10mm.

Spectral width and number of *fid* points. A spectral width sw = 8000 Hz was chosen, which at 600 MHz corresponds to approximately 13.3 *ppm*. 8000 points were collected from the *fid*.

Acceptable Spectrum for Data Acquisition. The linewidth of the water peak was used as a measure of acceptable spectrum and shimming. For the entire sample volume, the spectrum was acceptable when a linewidth under 40 Hz was achieved for the water peak. For the selected voxel, the spectrum was acceptable when a linewidth under 8 Hz was achieved for the water peak.

2.8.3 Step-by-Step Procedure

1. Sample was placed in holder and the CO_2 tank was turned on and adjusted so that gas flowed slowly into the sample holder. The holder was placed in the coil, and the coil was inserted into the magnet Next, the magnet was tuned.

2. (At the console) *spuls* experiment was started. Iteration was started through setting the offset frequency, calibrating the length of the 180° pulse and shimming until a linewidth under 40 Hz for the

water peak was achieved. This was good enough since a more accurate shim (over the selected volume) was necessary later in the acquisition.

3. Spin-echo or gradient-echo experiment was run to obtain images. The purpose of this step was to select a volume within the sample with good field homogeneity. Regions with uniform image brightness have acceptable field homogeneity (see selection in Figure 2.15). Several (coronal or sagittal) slices were imaged at a moderate resolution (eg, 64×64). A slice away from bubbles and as close as possible to the center of the sample was selected. A voxel was "planned", by selecting height, width and thickness, slightly below the media-gel interface. The voxel was then transferred to the MRSI experiment.

4. Within the MRSI experiment, the process "set offset frequency - calibrate (adiabatic pulse) pulse - shim" was repeated, in this case for the desired volume. In practice, calibration was usually needed only once, once the shim gives an acceptable spectrum. Again, water peak linewidth under 8 Hz for the selected volume was acceptable. This value allowed imidazole peaks to be clearly distinguishable. If this linewidth was achieved, but there was a pH gradient in the sample, only the C4,5-H imidazole peak was be visible, at around 7.2 ppm.

5. Once the shimming was satisfactory (water peak less than 8 Hz), phase encodings were started in the vertical direction (eg, 20) The number of averages (typically, 32×8, which can be achieved by assigning an array to the *nt* parameter) were selected. Next, the number of steady-state pulses (typically 4) needed to discard the first few repetitions until steady state is reached was selected.

2.8.4 Postprocessing of the Data

The acquired spectra contained a very large water peak, several orders of magnitude larger than the desired imidazole peaks used to estimate pH. Even though water and imidazole were spectrally well separated (the C4,5-H imidazole peak is located 2.4 ppm away from the water peak), the water signal was so intense that its tails often complicated visualization and phasing of imidazole peaks. However, the water signal was well modelled by a mixture of damped complex exponentials, and thus could be estimated (and removed) using harmonic-retrieval (HR) [31, 40, 41]. Moreover, automatic spectral quantization of the spectra could also be performed using HR-based methods [21].

The HR algorithm used in this project is Kung *et al.*'s method, known as HSVD in MR spectroscopy, and is based on a state-space formulation [41]. State-space methods model the N data points in vector $\mathbf{y}$ (the acquired fid samples) as a linear state-space model of order K. Using the following signal equation $y(t)$:

$$y(t) = \sum_{k=1}^{K} a_k e^{-d_k t + i2\pi f_m t} \tag{2.4}$$

If:

$$t = nT \tag{2.5}$$

$$z_k^n = e^{-d_k nT + i2\pi f_m nT} \tag{2.6}$$

Then:

$$y(t) = \sum_{k=1}^{K} a_k z_k^n \tag{2.7}$$

The $y_n = \sum_{k=1}^{K} a_k z_k^n$ data points are arranged in a Hankel matrix as follows:

$$\mathbf{H} = \begin{pmatrix} y_0 & y_1 & y_2 & \cdots & y_{M-1} \\ y_1 & y_2 & y_3 & \cdots & y_M \\ y_2 & y_3 & y_4 & \cdots & y_{M+1} \\ \vdots & \vdots & \vdots & & \vdots \\ y_{N-M} & y_{N-M+1} & y_{N-M+2} & \cdots & y_{N-1} \end{pmatrix} \tag{2.8}$$

HSVD performs the decomposition $\mathbf{H} = \mathbf{U\Sigma V^H}$, then truncates to a rank K matrix using the Eckart-Young theorem: $\mathbf{H_K} = \mathbf{U_K \Sigma_K V_K^H}$. The algorithm then obtains the least squares solution to:

$$\underline{\mathbf{U}}_\mathbf{K}\mathbf{Q} \approx \overline{\mathbf{U}}_\mathbf{K} \tag{2.9}$$

where $\underline{\mathbf{U}}_\mathbf{K}$ and $\overline{\mathbf{U}}_\mathbf{K}$ are obtained from $\mathbf{U_K}$ by omitting the last and first row of the matrix, respectively. It can be shown that (in the noiseless case) the eigenvalues of $\mathbf{Q}$ are the desired z_k. Each resulting z_k corresponds to an estimated Lorentzian peak in the spectrum, where $-\log|z_k|$ and $\angle z_k$ provide the damping factor (d_m) and frequency (f_m), respectively.

The amplitudes a_k of the peaks can be subsequently estimated simply by least squares fitting the estimated poles to the fid:

$$\mathbf{y} = \begin{pmatrix} z_1^0 & z_2^0 & \cdots & z_K^0 \\ z_1^1 & z_2^1 & \cdots & z_K^1 \\ \vdots & \vdots & & \vdots \\ z_1^{N-1} & z_2^{N-1} & \cdots & z_K^{N-1} \end{pmatrix} \begin{pmatrix} a_1 \\ a_2 \\ \vdots \\ a_K \end{pmatrix} \tag{2.10}$$

The effect of water removal by HSVD is shown in Figures 2.16 and 2.17.

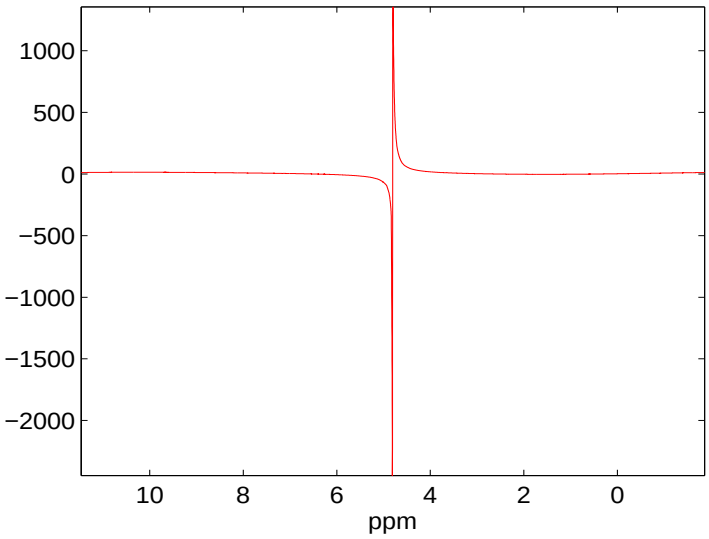

(a)

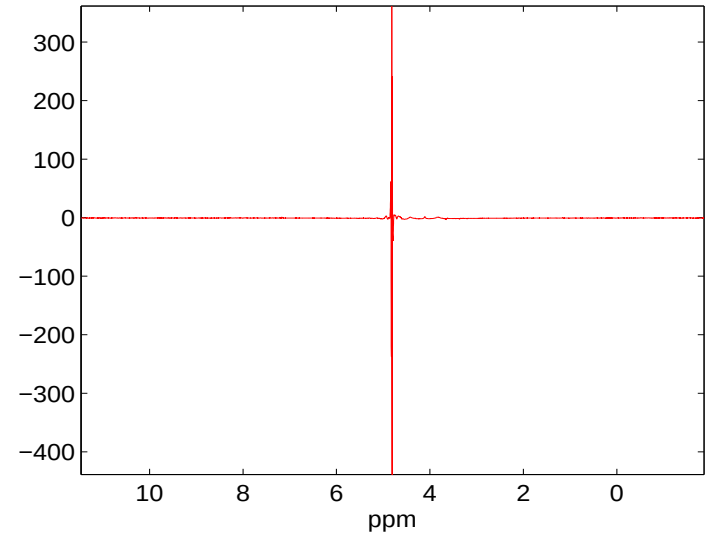

(b)

Figure 2.16: Effect of Water Peak Removal by HSVD. (a) Original Spectrum; (b) Water-removed Spectrum

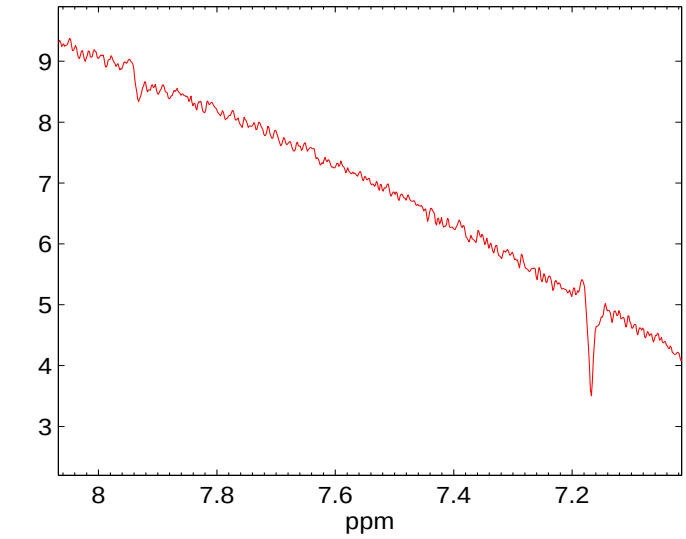

(a)

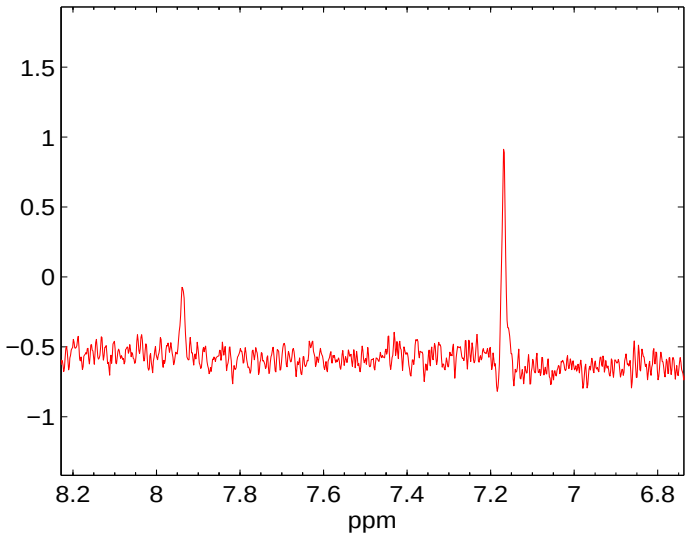

(b)

Figure 2.17: Effect of Water Peak Removal by HSVD. (a) Original Spectrum Zoomed into Desired Imidazole Peaks; (b) Water-removed Spectrum Zoomed Into Imidazole Peaks.

2.9 Mechanical Measurement

2.9.1 Establishment of Indentation Technique and Modulus Determination

The mechanics of contact between isotropic elastic solids were studied as early as 1881 by Hertz and Boussinesq in 1885 [4, 20]. Simple explicit expressions relating the force and indentation were developed for infinitely thick sample. In the later part of the last century, Sneddon used the method of integral transforms and obtained solutions for indentation of infinitely thick samples, while considering different indenter geometries [36]. Recognizing the importance of developing solutions for indentation of materials with finite thickness, several numerical computations were undertaken by Popov, Tu and Gazis, Dhaliwal and Rau and Chen and Engel [7, 9, 33, 39]. The work by Aleksandrov, which develops an integral transformation method, is applicable to material layers with finite thickness. However, it only applies to compressible materials; Poisson's ratio, $\nu \neq 0.5$ [3]. The solutions proposed by Hayes et al. are valid for incompressible materials ($\nu = 0.5$) [19]. More recently, Yang and Chadwick found that the force-indentation relation for thin layers of material depends on whether the sample is bonded or not to the substrate [6, 43]. In the case of indentation of finite thickness materials, the intrinsic nonlinear relation between the contact area, pressure profile and force leads to an integral equation that is solved using numerical schemes. In an attempt to create an easier approach, Dimitriadis et al. constructed a Green's function for a finite thickness bonded material and used it to compute approximate indentations. He used the method of images to obtain an approximate solution for a material unbonded to the substrate [10]. The integral equations were rewritten into a hierarchy of simpler integral equations and the analytical solutions were used to obtain correction terms to the classical Hertz solution known for an infinitely thick sample. Equation 2.11 from the study conducted by Dimitriadis et al. shows the relation between the applied contact force, depth of indentation and accounts for the finite thickness of the sample being tested and is valid for all values of Poisson's ratio [10].

$$F = \frac{4E}{3(1-\nu^2)} R^{\frac{1}{2}} \delta^{\frac{3}{2}} \left[1 - \frac{2\alpha_0}{\pi}\chi + \frac{4\alpha_0^2}{\pi^2}\chi^2 - \frac{8}{\pi^3}(\alpha_0^3 + \frac{4\pi^2}{15}\beta_0)\chi^3 + \frac{16\alpha_0}{\pi^4}(\alpha_0^3 + \frac{3\pi^2}{5}\beta_0)\chi^4 \right], \tag{2.11}$$

,where $\chi = \frac{\sqrt{R\delta}}{h}$ is a non-dimensional quantity relating the radius of the indenter, R, depth of indentation, δ and height of the sample, h. The terms α_0 and β_0 are functions of the Poisson's ratio of the material, ν, and differ when the material is bonded or unbonded to the substrate. The following, Equation 2.12, is for a sample which is bonded and Equation 2.13 is for a sample which is unbonded to the substrate.

$$\alpha_0 = -0.347\frac{3-2\nu}{1-\nu}, \qquad \beta_0 = 0.056\frac{5-2\nu}{1-\nu} \tag{2.12}$$

$$\alpha_0 = -\frac{1.2876 - 1.4678\nu + 1.344\nu^2}{1-\nu}, \qquad \beta_0 = \frac{0.6387 - 1.0277\nu + 1.5164\nu^2}{1-\nu} \tag{2.13}$$

The factor in front of the bracket in Equation 2.11 is the Hertz solution for indentation of a semi-infinitely large sample. The expression in the bracket is the correction factor that depends on the thickness of the sample; it approaches 1 as the thickness of the sample approaches infinity. The decrease in thickness of the sample leads to a larger value and hence a larger contact force for the same depth of indentation. This behavior represents the apparent stiffening effect observed when testing thin samples.

A vast majority of biological samples have a Poisson's ratio, close to 0.5. For such materials Dimitriadis et.al. provide a simpler expression relating the contact force and depth of indentation which is given by Equation 2.14 for a sample which is unbonded and Equation 2.15 for a sample which is bonded to the substrate.

$$F = \frac{16E}{9}R^{\frac{1}{2}}\delta^{\frac{3}{2}}[1 + 0.884\chi + 0.781\chi^2 + 0.386\chi^3 + 0.0048\chi^4] \tag{2.14}$$

$$F = \frac{16E}{9}R^{\frac{1}{2}}\delta^{\frac{3}{2}}[1 + 1.133\chi + 1.283\chi^2 + 0.769\chi^3 + 0.0975\chi^4] \tag{2.15}$$

The use of microspheres as indenters has been investigated by Mahaffy et al. and Dimitriadis et al. and have been shown to avoid damaging delicate biological materials. Also, the measured Young's modulus using atomic force microscopy technique has been verified to be in good agreement with those obtained from macroscopic tests [10, 30].

Determination of Modulus Correction Factor

In this study, an indentation test is performed on a matrigel sample bonded to a container. Matrigel is used as a scaffold material for cell culture and is expensive when used in large amounts. Hence, an indentation test is chosen to estimate the modulus. Polymeric media, such as gels, are close to being incompressible. In comparison to the semi-infinitely large sample for which the Hertz solution is appropriate, the current testing configuration is influenced by sample geometry along both depth and lateral dimensions. Equation 2.15 represents the force-displacement relation for indentation of a bonded incompressible sample and has been used in our study to account for the finite height of the sample.

To study the effect of lateral confinement of finite-diameter samples, three different sized cylindrical containers with diameters of 12mm, 22mm and 31.75mm were considered. Gels with height of 4.5mm were tested using the 5mm diameter indenter.

Equation 2.15 is rewritten to solve for the Young's modulus using each pair of contact force, F, and indentation depth, δ measured during the indentation experiment (Data shown in Figure 2.18). The modulus generated using the raw data is noisy at small displacements (Figure 2.19) where the relative uncertainty in the force is large. For large indentation depths, greater than 1mm, the apparent stiffening is due to the boundary effects coming into play, depending on the container size.

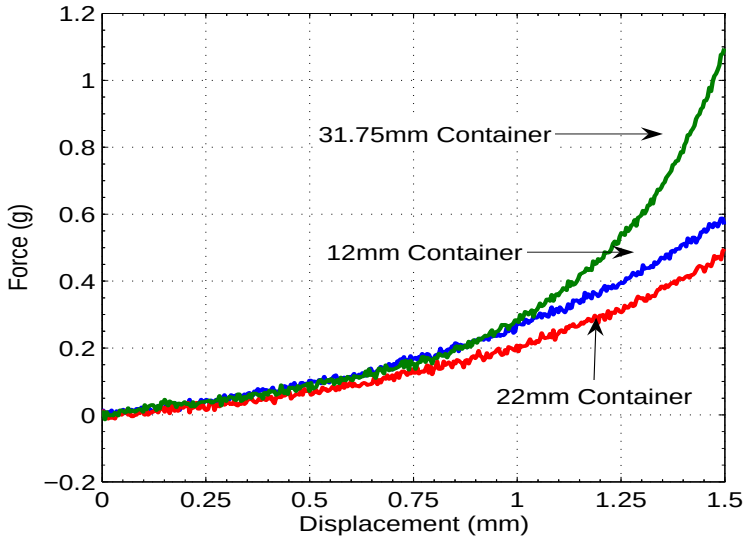

Figure 2.18: Force vs. Displacement for Three Different Diameter Containers

The results of Figure 2.19 indicate that at an indentation depth of 0.8mm, the modulus plateaus and is found to be the same for the 22mm and 31.75mm diameter containers. It is concluded that containers of at least 22mm diameter can be used to report values for the modulus measurement of matrigel without the effects of boundaries from the container.

To minimize the matrigel volume (and reduce costs), the 12 mm diameter sample container was instead selected and a correction factor to estimate the sample elastic modulus was applied. The correction factor is the ratio of modulus estimates, E, (see Figure 2.20) at a displacement of 0.8mm: $C = \frac{E_2 2mm}{E_1 2mm}$. To obtain the modulus estimates, the force versus displacement curves for the 12mm and 22mm diameter containers were fit using a cubic polynomial. The cubic equations are given in Equations 2.16 and 2.17 respectively.

$$f = 0.088d^3 - 0.019d^2 + 0.15d - 0.0056 \tag{2.16}$$

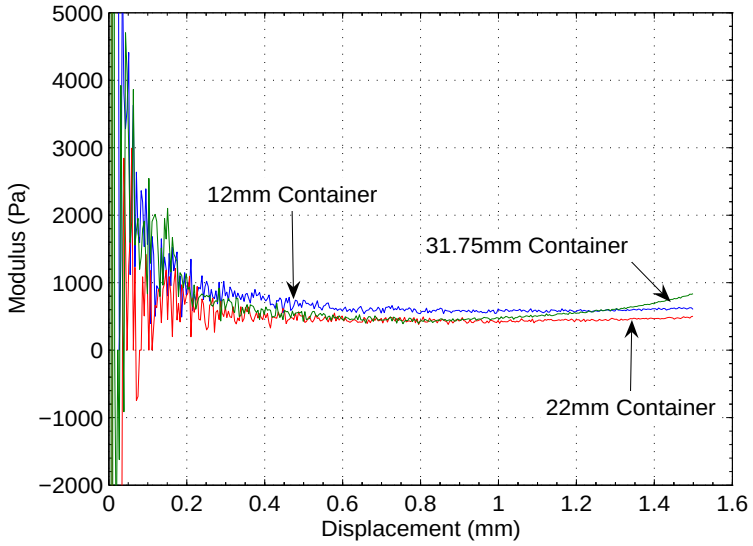

(a)

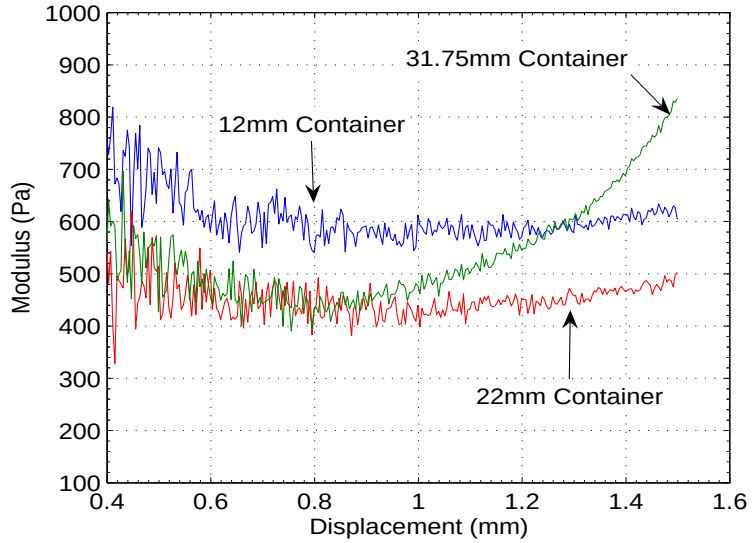

(b)

Figure 2.19: (a) Modulus vs. Indentation Depth for Three Different Diameter Containers; (b) Closeup of Graph (a)

$$f = 0.028d^3 - 0.023d^2 + 0.12d - 0.003 \tag{2.17}$$

These fits were then used to calculate the modulus data from Equation 2.15, as it gives a much smoother curve. At 0.8mm displacement, the modulus for the 12mm diameter container is 560 Pa and the modulus for the 22mm diameter container is 460 Pa (Figure 2.20). Therefore, the correction factor is 0.82. This established correction factor is used in the six day mechanical study performed in the small container on

matrigel with and without cells.

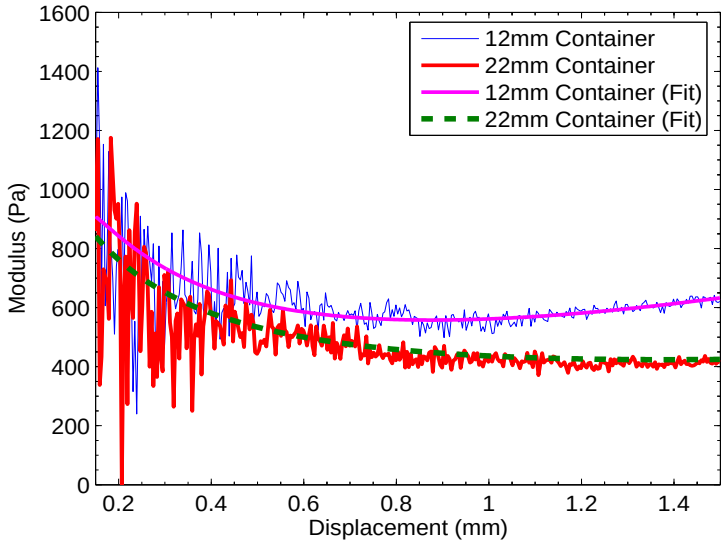

Figure 2.20: Modulus vs. Displacement using Fit Data for 12mm and 22mm Diameter Containers

The cubic curve fit was applied to all force versus displacement data obtained in experimentation. The modulus curve was then generated from this fit.

2.9.2 Study Details

A five day study of the elastic modulus change in matrigel with NIH 3T3 mouse fibroblasts growing inside was conducted. Eighteen samples were made on day zero in 12mm diameter 12-well plate inserts, as described previously in the sample preparation section. The samples were maintained in an incubator and 1ml of media on top of the sample was changed each day. Each day, starting with day zero, the elastic modulus was determined on three separate samples.

2.9.3 Setup

Matrigel sample elastic moduli were determined in an environment that mimicked that of the incubator. The sample was placed in an environmental tank controlled to $37°(\pm 1°)$ C with a continuous flow of air containing 5% CO_2, 10% O_2 and balanced with N_2. Since the mechanical properties of matrigel depend on environmental factors, the incubation environment was maintained. The heat was generated using a slow flow of heated water through the tank surrounding the space where the sample was contained. The water was circulated and heated with an outside bath. The slow air flow came into the tank above the sample. To control humidity, dri-rite crystals were placed inside of the sample area of the tank. A humidity/temperature

probe was placed through the lid of the tank next to the sample to manage/detect conditions. The entire tank and tester set-up was contained within a clear plastic environment chamber to reduce outside air current and temperature changes. A small space heater was placed inside of the environment chamber and used before testing to heat the air and probe to prevent condensation on the probe. Diagrams of the setup are shown in Figures 2.21, 2.22, and 2.23.

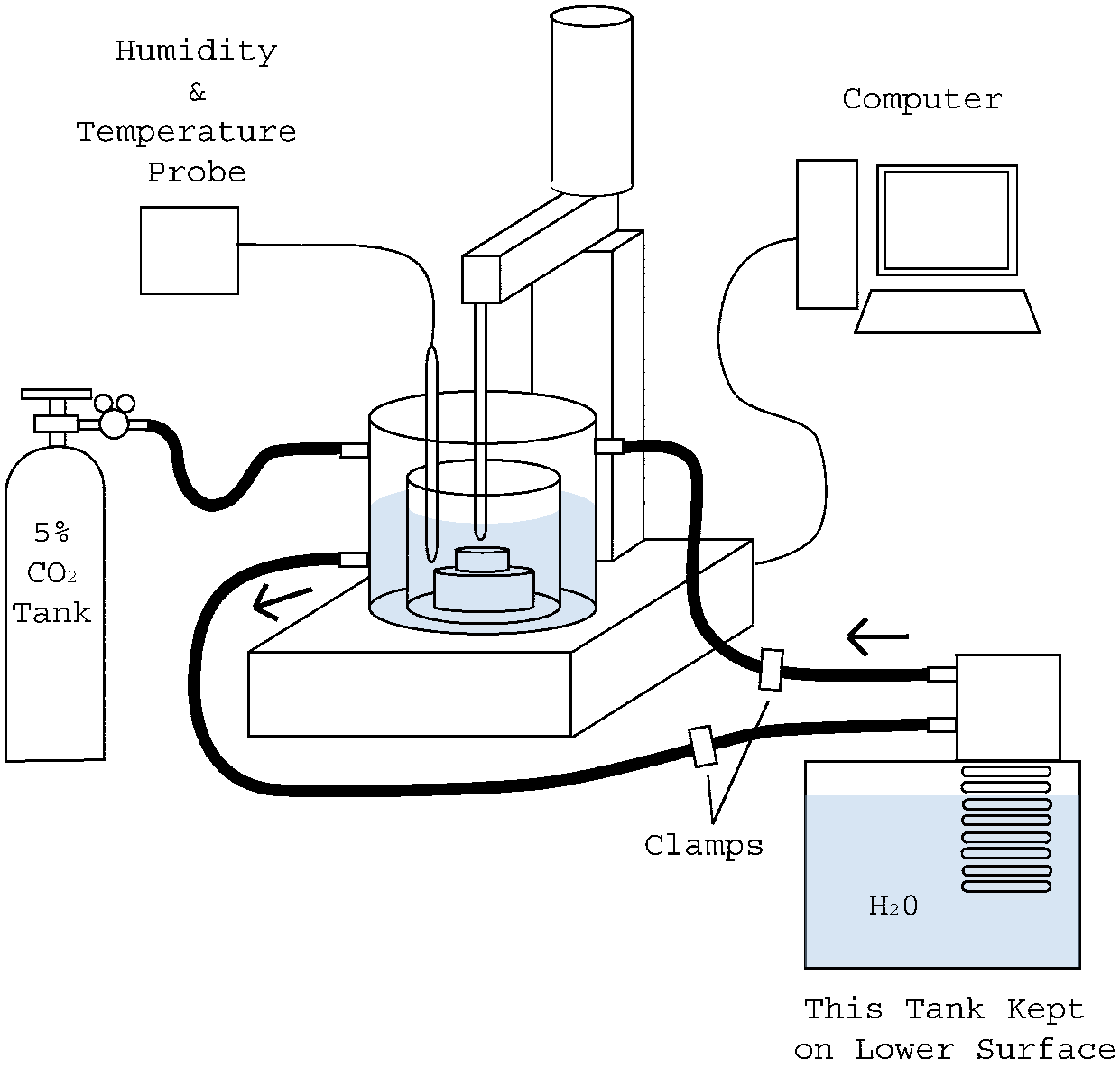

Figure 2.21: Mechanical Measurement Experimental Setup

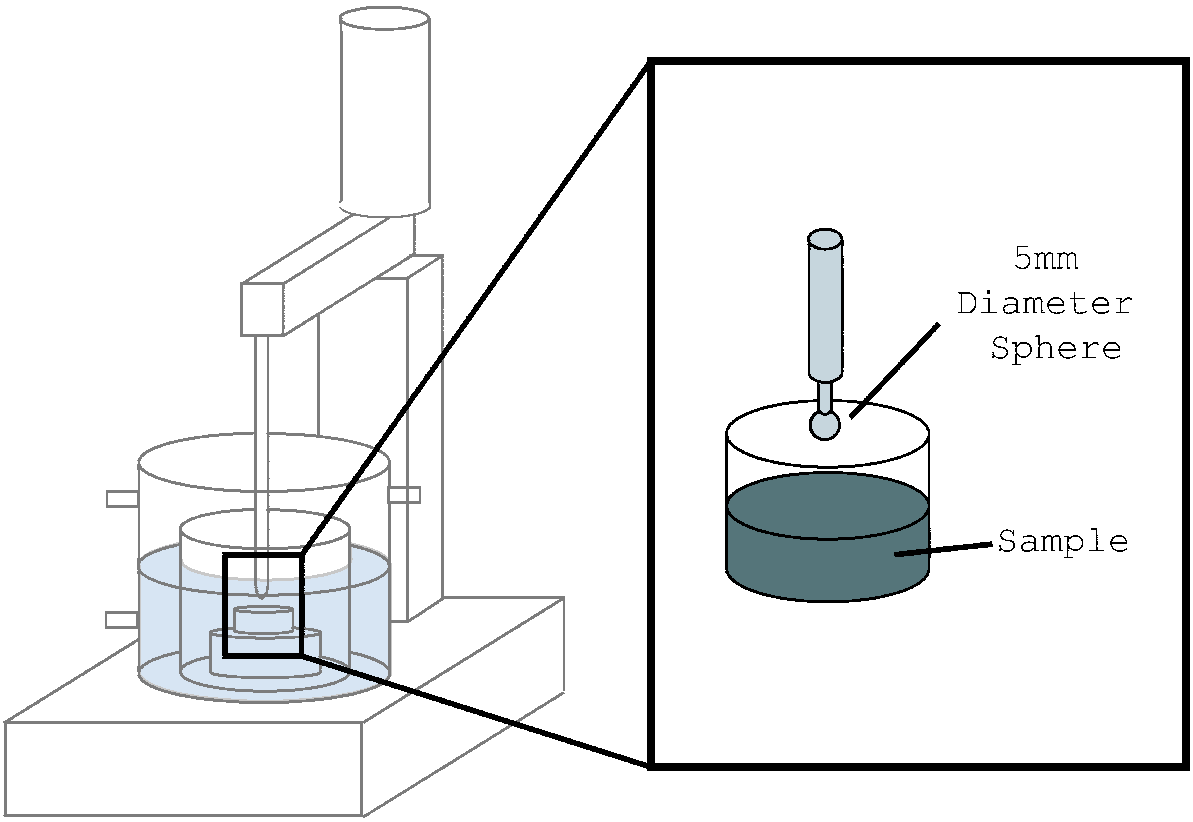

Figure 2.22: Mechanical Measurement Setup Detail A

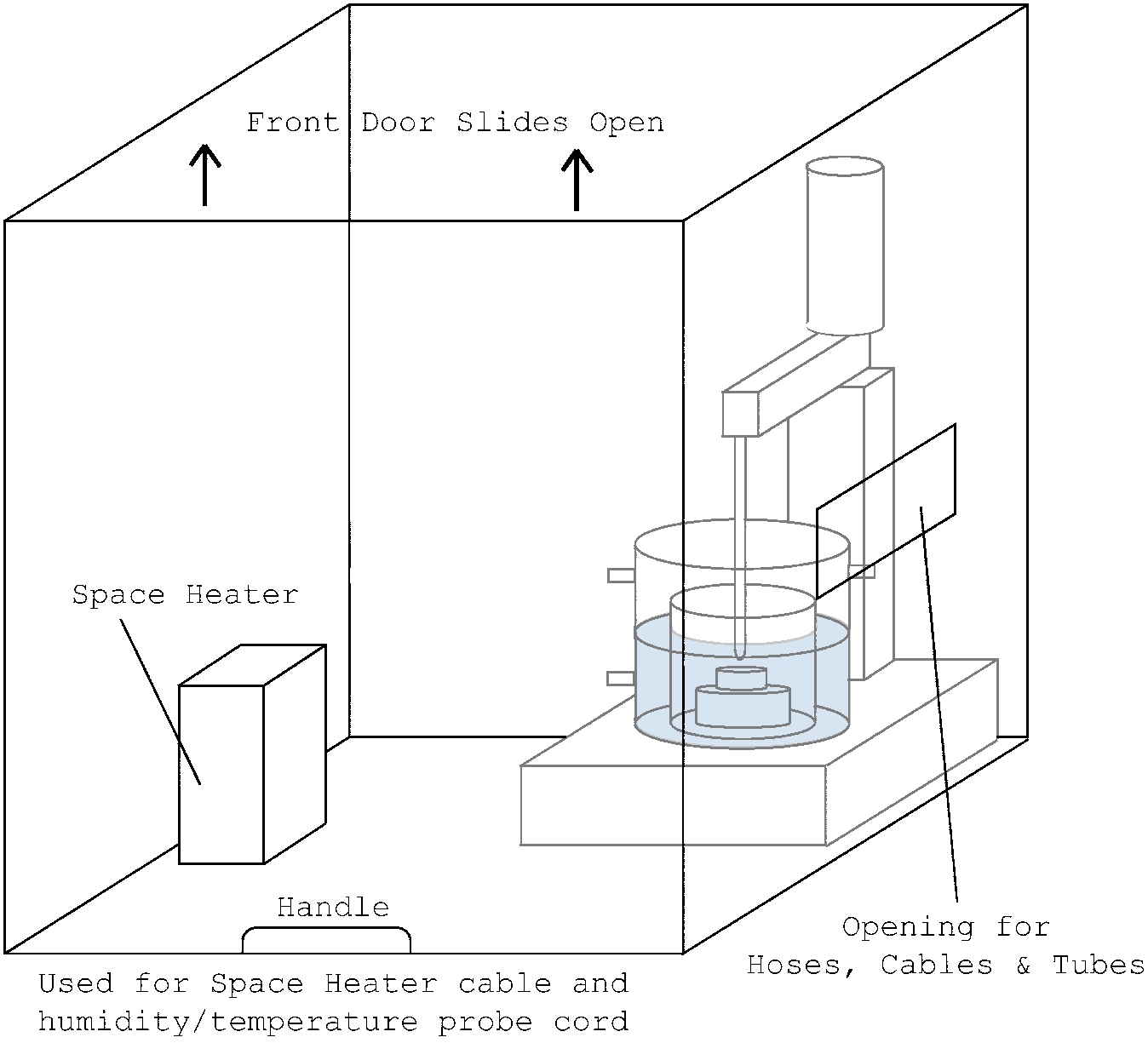

Figure 2.23: Mechanical Measurement Experimental Setup Detail B

2.9.4 Experimental Procedure

A TA.XT Plus Texture Analyzer (Stable Micro Systems, UK) was used for mechanical modulus determination of samples using a stainless steel 5mm diameter spherical probe to compress the samples 1.5mm. The data used for modulus determination was at 0.8mm indentation. Prior to experimentation, the Texture Analyzer was calibrated to the height of an empty container in order to later determine the height of the

sample. A 1kg load cell was either re-calibrated with a 5g calibration weight or checked with the weight for accuracy of readings. For experimentation, the sample was taken from the incubator and placed in the environmental tank for 10 minutes prior to indentation. This allowed the sample to reach equilibrium with the temperature and CO_2 concentration. During this time, the space heater was running to prevent condensation from occurring during measurement. The heater was turned off before the test in order to prevent air current artifacts in the force measurement.

The surface of the sample was detected by lowering the probe at a rate of 0.05mm/sec at 0.1mm increments in the program. Once the force reached -0.1g (from surface tension), the probe was lowered 0.1mm and a 5 cycle triangle wave indentation test at 0.05mm/sec was run. Force and distance were automatically recorded at a sampling rate of 12.5 points per second by the TA.XT program. The data analyzed for elastic modulus determination was the first cycle of indentation (loading).

2.10 Optical Coherence Tomography

Optical coherence tomography is a technique that has emerged with the potential to overcome many limitations of invasive and often destructive traditional methods of studying cell activities in a three dimensional structure. Invasive techniques, such as histology and scanning electron microscopy lack real three dimensional information and often make correlations between structure and function difficult [37]. OCT provides high resolution, cross-sectional tomographic imaging of internal microstructure in materials and biological tissues by measuring the intensity of back-reflected near-infrared light [13]. It allows imaging at cellular resolutions without the use of exogenous fluorophores. Because near-infrared light is scattered less than visible light, OCT allows non-invasive deep imaging penetration, 2-3mm, within highly scattering tissues [37]. OCT's initial application was for imaging of the eye beginning in 1991 [13]. In vivo tomograms of the human optic disc and macula were first done in 1993. Due to more recent advances, OCT can now be used to image non-transparent tissues, with the depth of view being limited by optical attenuation from tissue scattering and absorption [13]. OCT was used in this study to locate cells within a matrigel three dimensional geometry, specifically focusing on cell location in the vertical depth. By scanning and taking images across the gel, three dimensional information was obtained.

The OCT system used for imaging was a fiber-based spectral-domain system using an ND:YVO4-pumped titanium:sapphire laser as a broad-bandwidth optical source. It produced 500mW of average power and approximately 90-fs pulses with an 80MHz repetition rate at an 800nm center wavelength. The bandwidth is approximately 115nm, which provides an axial resolution of 3μm. The sample light was collimated through

a 40mm focal length achromatic lens, which provided approximately 16μm lateral resolution. Figure 2.24 displays the OCT system setup.

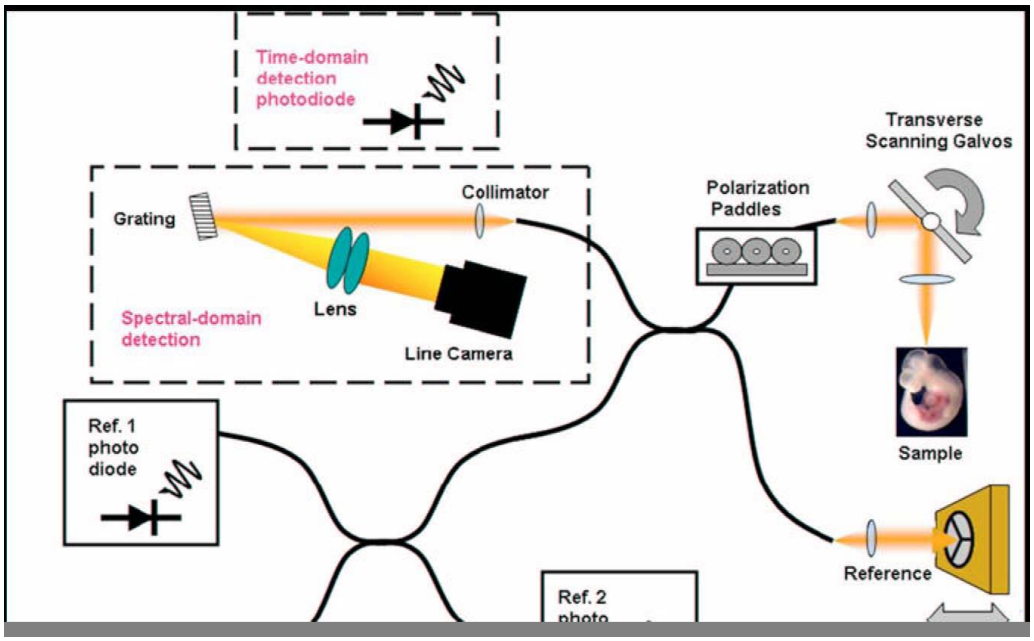

Figure 2.24: Diagram of OCT system [29]

OCT was used to visualize fibroblasts in matrigel after 3 days of culture in the 12mm diameter cell culture insert geometry. The gel was 1ml in volume. Three dimensional scans were done over a 3mm width x 2mm depth x 3mm elevation. 200 images were taken across the 3mm elevation with final images having a size of 3mm in width, 2mm in depth and 0.015mm in elevation.

Chapter 3

Results

3.1 Cell Density and Migration in Matrigel

A study was conducted to determine proliferation and migration patterns of fibroblast cells in the matrigel over 5 days. The results of live cell count, shown in Figure 3.1 (a), show that the cells grew exponentially with a doubling time of 1.8 days. Three samples were counted each day and the error bars in Figure 3.1 is the standard deviation. This variability can result from several steps in the cell density study procedure. This includes the estimation of cells added to the gel initially, variations in growth rate, and loss of cells during the dispase and centrifugation steps in the recovery. The coefficient of correlation of the exponential fit to the data is $r^2 = 0.983$.

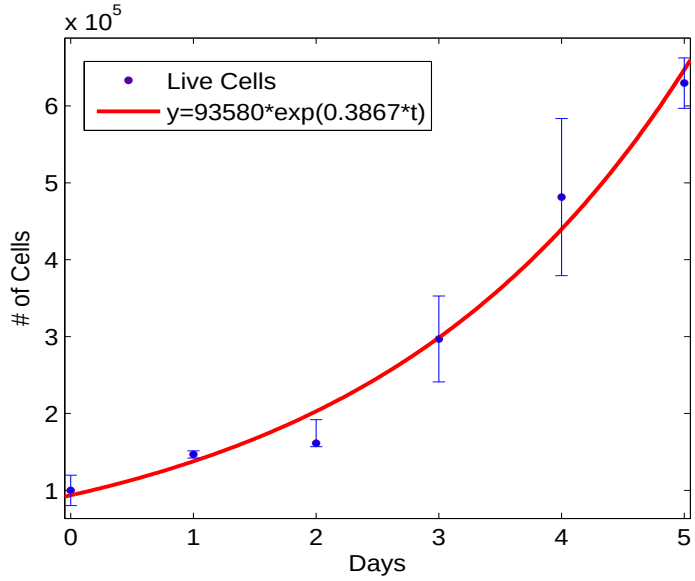

Figure 3.1: Average Number of Live Cells in 1ml Matrigel Samples Estimated over Time. Error bars denote ± standard deviation of the mean values.

The dead fibroblasts in the matrigel were also counted over 5 days. The results, shown in Figure 3.2, show that the number of dead cells did not increase until day two of culture. This is the same time frame

in which the cells started to proliferate inside of the gel. It appears that most cell death occurred between days 2 and 4. These may be cells that did not survive the acclimation time period. Cell survival could be related to initial location in the gel; media was added only to the top surface. The rate of cell death may have decreased after 4 days because cells initially located far from nutrients would already have died. To get a sense of how cell location affects survival and proliferation, we examined optical coherence tomography images of a sample after 3 days of culture.

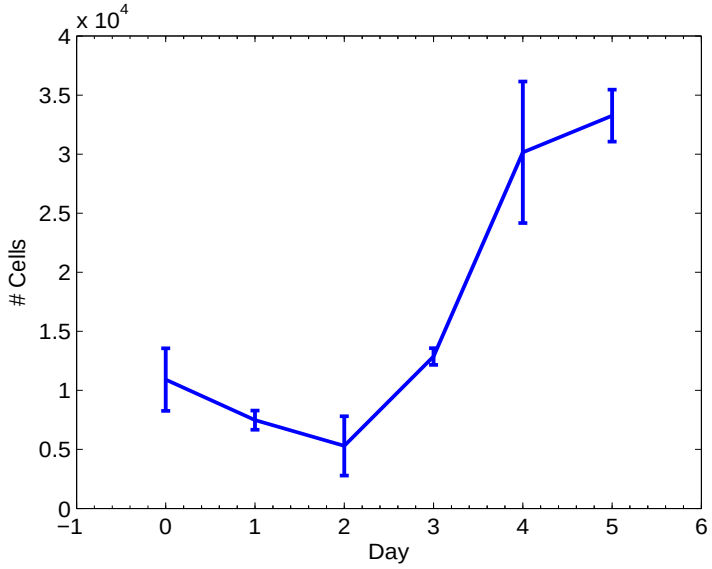

Figure 3.2: Dead Cell Count with Time. Error bars denote ± standard deviation of the mean values.

Optical coherence tomography images were taken of a matrigel sample with fibroblasts that had been culturing for 3 days. The sample was prepared in the same manner as the gels for the mechanical and cell density studies as described in the methods chapter. Initial cell density was 100,000 fibroblasts/ml of matrigel and the cells were homogenously mixed throughout the sample. The sample was 5.7mm thick. OCT images were taken through the bottom and top surfaces of the sample to estimate cell distribution versus depth.

Cells were counted in the OCT image shown in Figure 3.3 to estimate the total number of cells/ml of matrigel. The matrigel volume imaged in 3.3 is approximately 3mm wide and 2mm high in the image plane and 15μm thick. The total volume of the image plane is 9*10^{-5}ml. Thirty two cells are visible in Figure 3.3 and 28 cells are seen in an adjacent scan in Figures 3.4. Both values were obtained from images of the bottom of the matrigel sample. To make an estimation, it is assumed this density of cells is not a maximum or a minimum, but mean of the spatial average. We estimate therefore, that there are $30/9 * 10^{-5} = 333,000$cells/ml on day 3. On day 3, 296,859 fibroblasts were measured through cell retrieval.

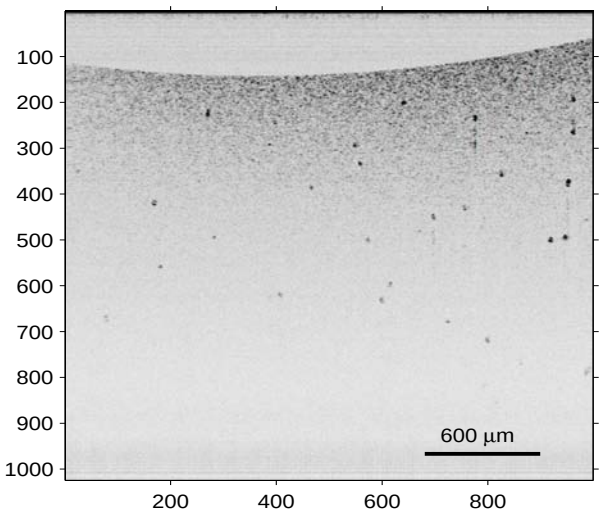

Figure 3.3: OCT Image on Day 3: Bottom of Sample

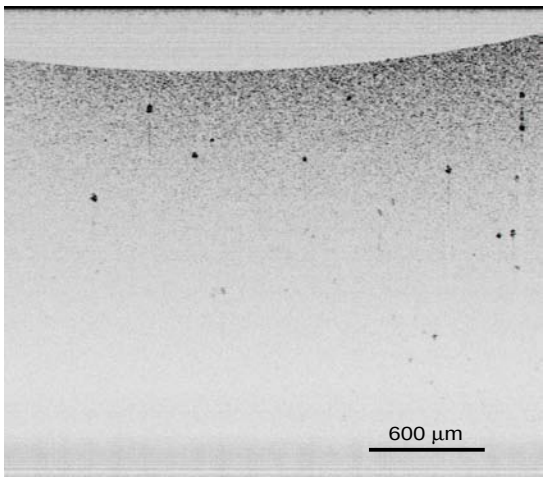

Figure 3.4: OCT Image on Day 3: Bottom of Sample with Correlation to Cell Density Count

Images were also taken from the top of the same sample. There were fewer cells at the top of the gel on day 3 than at the bottom. A representative image from the top is shown in Figure 3.5.

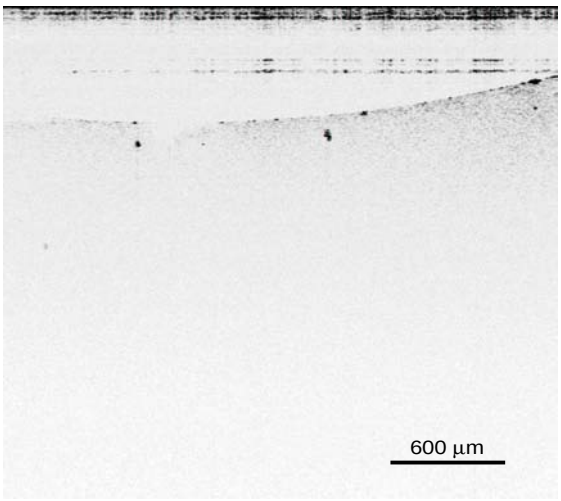

Figure 3.5: OCT Image on Day 3: Top of Sample

OCT imaging has a limited depth of penetration, 2mm in this instance. Imaging of both the top and bottom surfaces allowed visualization of cells through most of the sample, with approximately 2mm of gel in the middle that could not be imaged. Despite this limited depth of focus, it was clear that cells were attracted to both the top and bottom surfaces.

Sixty six images from both the top and bottom of the sample were visually analyzed for cell location estimation throughout the gel depth. Average number of cells in 0.4mm sections in the images were calculated. The results are shown in Figure 3.6. The data shows that there are more cells at the top and bottom surfaces of the gel. This indicates that there are two driving forces for cell migration in the vertical direction. Medium was located at the top of the gel, so the cells were attracted towards this area for nutrients. The cells were drawn more to the bottom surface despite the location of the medium , therefore the 12% over estimation of cell number is reasonable to expect. This data also shows that the medium can diffuse through the 5.7mm of matrigel. Otherwise, cells would not proliferate at the bottom of the gel. The bottom of the cell culture insert is tissue culture treated to promote adherence and proliferation. This is believed to be the reason cells are attracted to this surface.

Fibroblast migrate through the matrigel by breaking down the matrix, rather than moving through pores. As seen in SEM imaging, matrigel pores are between 100 and 700nm in diameter. The NIH 3T3 fibroblast cell is approximately 50μm in size and could not fit through these pores. Fibroblasts are known to secrete

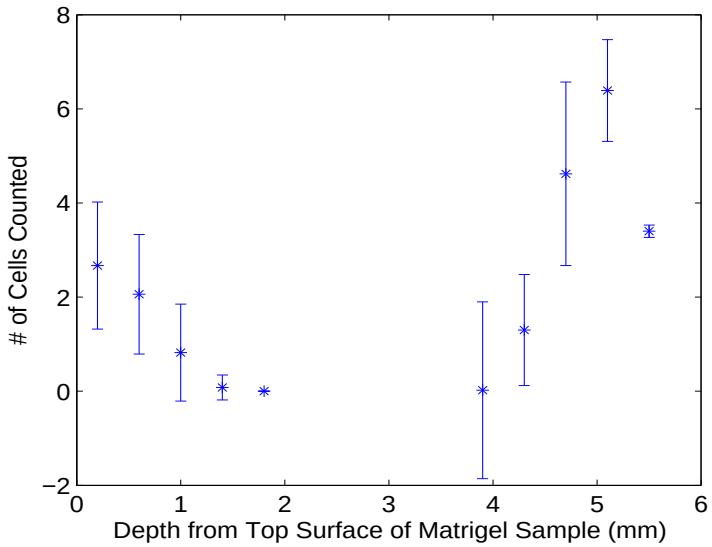

Figure 3.6: Cell Gradient with Depth as Estimated from OCT Images. Error bars denote ± standard deviation of the mean values

matrix metalloproteinases (MMPs) that break down extra cellular matrix (ECM) proteins to regulate ECM homeostasis and turnover [23]. This turnover of ECM is known to occur in the wound healing process. Stromal fibroblasts produce MMP-2, which is responsible for synthesis, deposition and remodelling of the ECM to support cell ingrowth and migration in healing wounds [32]. It is likely that the fibroblasts in the matrigel used this method of degradation and remodelling of the matrix to migrate through the matrigel toward the surfaces.

3.2 MRSI pH Measurements

The MRSI technique applied in this study allowed us to estimate pH as a function of depth in the matrigel over 0.5mm voxels. Recall that these matrigel samples are placed into a 12mm diameter glass tube that is 75mm long. The phase encoding direction is along the tube length. Spectra from 20 voxels, beginning at the top of the gel, were obtained for the matrigel-cell samples. In each sample data set, there were several voxels where the imidazole peaks were not clearly defined and the pH value was indeterminable. However, in each case, enough of the slices showed evident peaks and allowed pH measurement. This data is shown in Figure 3.7. A gradient is present in the vertical direction with a lower pH at the top of the gel that increases with depth. A linear curve has been fit to each set of data.

The data shows the steepest gradient (slope = 0.044mm^{-1}) at day 1 of culture. The gradient slope drops on day 2 (slope = 0.029mm^{-1}) and then again on day 3 (slope = 0.15mm^{-1}) . There is some variability in

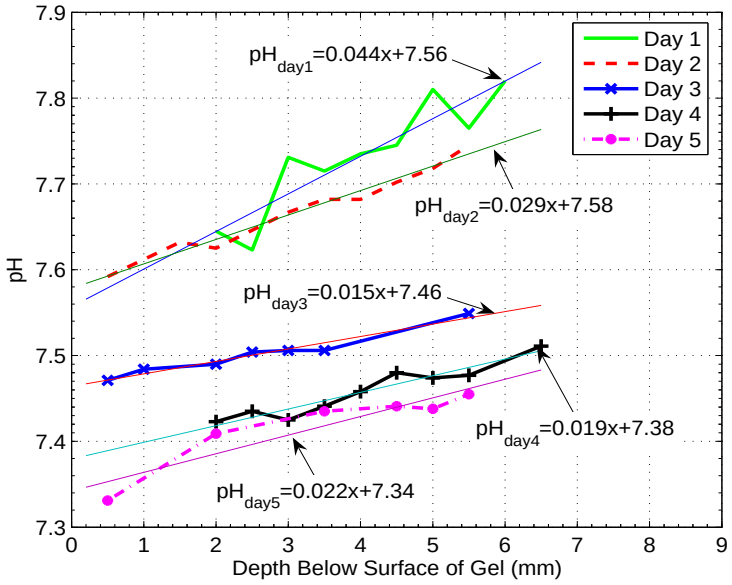

Figure 3.7: pH Gradient with Depth in Matrigel-fibroblast Samples as Estimated with MRSI

the pH gradient between days 3 and 5 (between 0.15 and 0.022), but it is clear that the gradient decreases with time initially and then stabilizes beginning on day 3.

Matrigel with 50mM of imidazole is basic with a pH of 8.4. Media with buffering capacity and a pH of 7.4 was added to the top surface of the gel. Consequently, the initial gradient can be attributed to the equilibration of medica and matrigel pH. As the media seeps into the top of the matrigel through the pores, it creates a gradient of lower pH at the top that increases through the 9mm depth of the voxel of interest.

By day 3, cells are proliferating and thus metabolizing to produce acidic products that lower the overall pH. A small gradient persists through day 5 since the medium is replaced daily.

Gradients of pH were also present in the control data. These samples were prepared and measured in the same manner, except no cells were introduced. The data and linear fits are shown in Figure 3.8. Again, the gradient has the largest slope on day 1 and decreases with time. The gradient drops to 0.015mm^{-1} by day 4. Again, the media seeping into the more basic matrigel causes this gradient just as in the matrigel-fibroblast samples.

The above MRSI pH data was averaged over depth on each day for the matrigel-fibroblast and control matrigel samples. The data are shown in Figure 3.9. These are the average pH values for 0.14ml samples, as explained in the methods chapter.

The graph shows an initial decrease in pH from day 1 to day 3 in both sets of data. This decrease continues for the matrigel samples containing cells until day 5. On day 4 of the control measurements, the

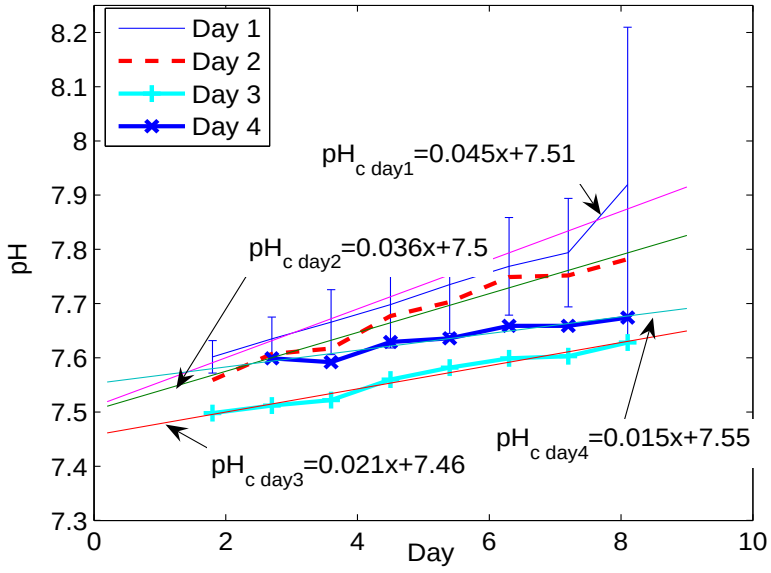

Figure 3.8: pH Gradient with Depth in Matrigel without Cells (Control Samples). On day 1, three samples were measured; the error bars denote ±1 standard deviation

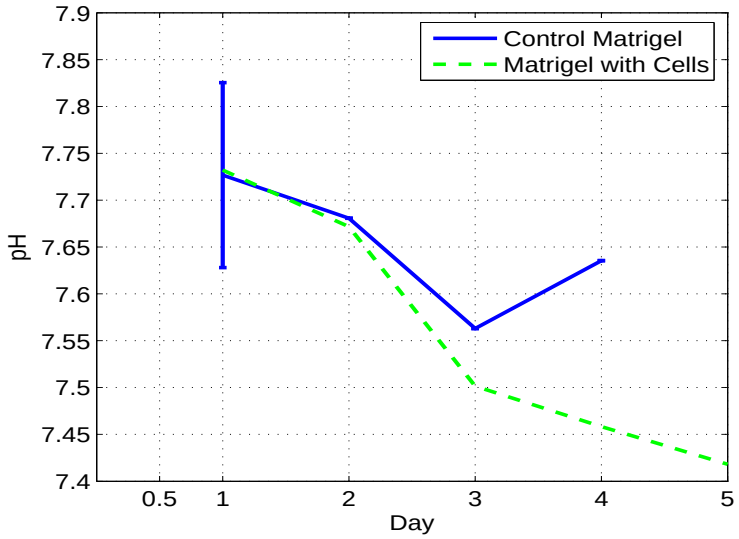

Figure 3.9: pH of Matrigel-Fibroblast and Matrigel Control Samples. On day 1, three samples were measured; the error bar denotes ±1 standard deviation

data shows an increase in pH by 0.7 from day 3. This data point shows that there may not be a decreasing trend in pH after day 3. It is expected that by this point in time, the pH of the gel would stabilize with the $5\%CO_2$ environment. It is reasonable to believe that after 2-3 days of incubation in $5\%CO_2$ and 37°C, the control gel would reach a stable mechanical and biochemical state. Therefore, the pH range of the stable gel may in fact be somewhere in the range of 7.6. Data were not obtained on day 5 for the control matrigel. On day 5 of measurement, the left imidazole peak, which represents the C2-H, was not visible in the spectrum and therefore the pH was undeterminable. Reasons for the peak disappearance will be addressed in the discussion section.

The pH change in matrigel due to the culture of fibroblast cells can be determined through subtraction of the control from the experimental data. The results of this analysis are shown in Figure 3.10.

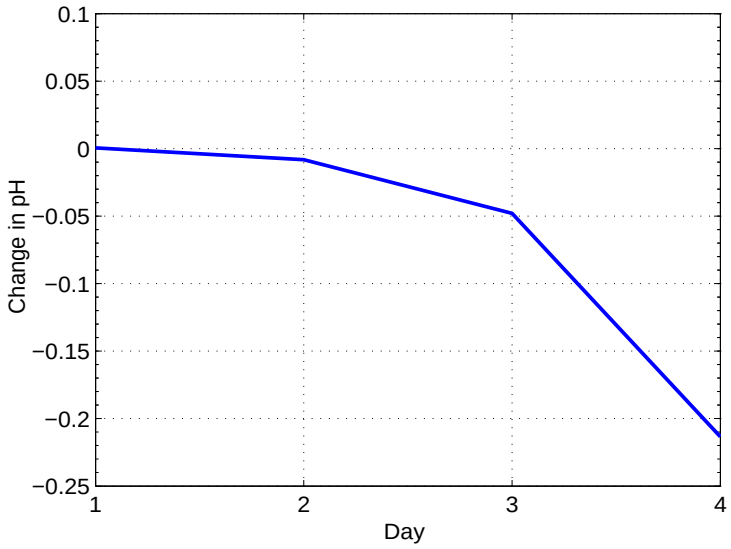

Figure 3.10: Change in pH caused by NIH 3T3 Fibroblasts with Culture Time

From this figure, it is evident that the cells decreased the pH of the matrigel 0.22 by day 4. The decrease in pH of the matrigel with fibroblast culture is expected. It has been shown that NIH 3T3 fibroblasts produce lactate as a product of glucose and glutamine metabolism in culture [28]. The lactate is secreted by the cell along with a proton (H^+), which causes a decrease in extracellular pH [27]. In vivo, this process would not normally cause a decrease in extracellular pH due to the close proximity of blood vessels which take up the extra protons in the tissue to maintain a pH of 7.4. In this experimental setup, there is no acid sink and therefore, the pH decreases in the extracellular matrix, or matrigel, surrounding the fibroblasts.

3.3 Mechanical Measurements

The elastic modulus curves for the matrigel with fibroblast culture along with control matrigel for a 6 day study are shown in Figures 3.11 and 3.12 respectively. Figure 3.11 shows representative modulus curves from each of the 6 day samples. In actuality, 3 samples were tested on each day for the study and the error bars are shown in Figure 3.13. Only one sample was tested each day for the control.

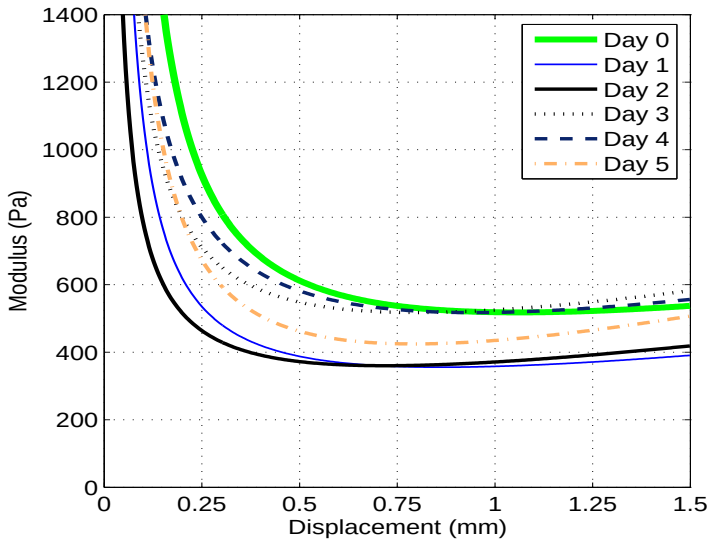

Figure 3.11: Modulus of Matrigel Cultured with Fibroblasts

The modulus for each data set was extracted from the plateau region of the curve, which occurred in a displacement of 0.8mm for all samples. The modulus was corrected for the 12mm diameter sample container using the 0.82 correction factor as described in the methods section. The results for both control matrigel and matrigel cultured with fibroblasts are shown in Figure 3.13.

The control gel decreased in stiffness by 51% over the first 2 days of incubation. The modulus remained approximately constant between days 2 and 5. This result is expected due to the time it takes for equilibration of the gel with the environmental conditions of $5\%CO_2$ and 37°C. It is evident from the data that the acclimation time is approximately 2 days.

The modulus data for the matrigel with fibroblasts culturing inside decreases 19% from day zero to day 2. This initial decrease in stiffness is again due to the equilibration of the gel with the incubation conditions. However, the decrease is less than that of the control, which indicates that there is a stiffening mechanism competing. The modulus increases from day 2 to day 4 by 29%.

The change in modulus caused by fibroblasts culturing inside of the gel can be determined by subtracting the value of the modulus of the control from that of the gel with the cells. This data is shown in Figure

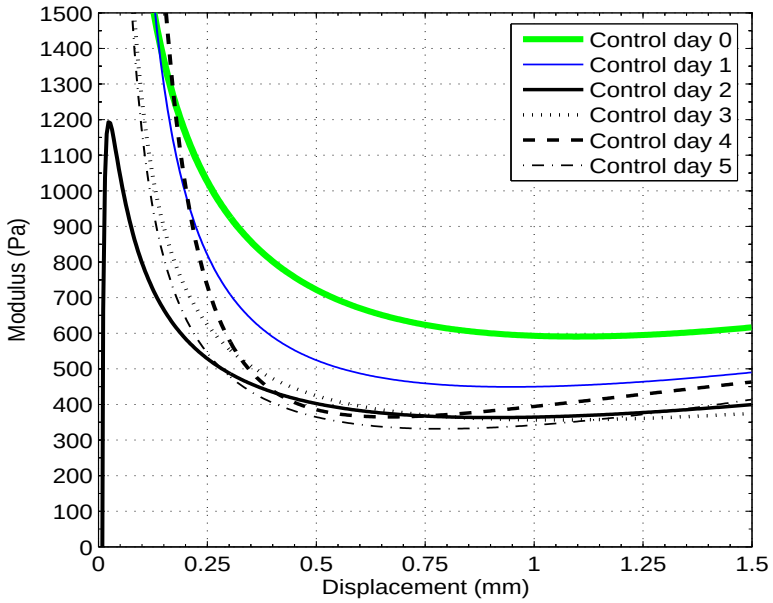

Figure 3.12: Modulus of Control Matrigel Samples

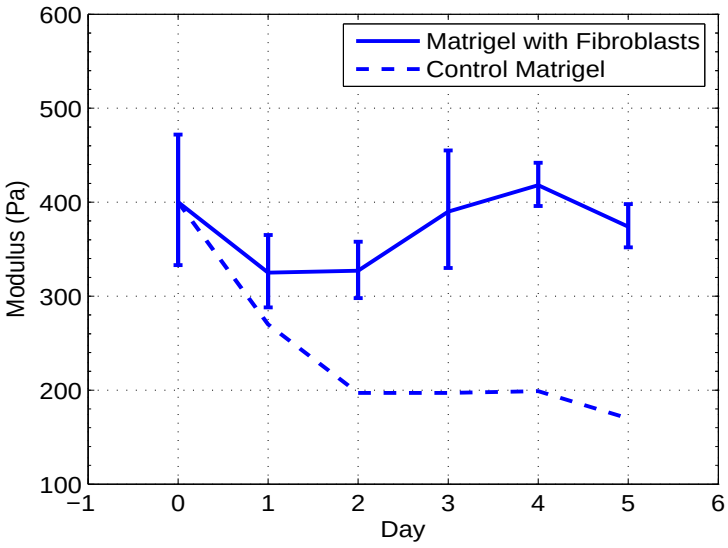

Figure 3.13: Modulus of Control Matrigel and Matrigel with Fibroblasts with Standard Deviation Error Bars

3.14. The cells stiffened the gel a maximum of 219 Pa by day 4.

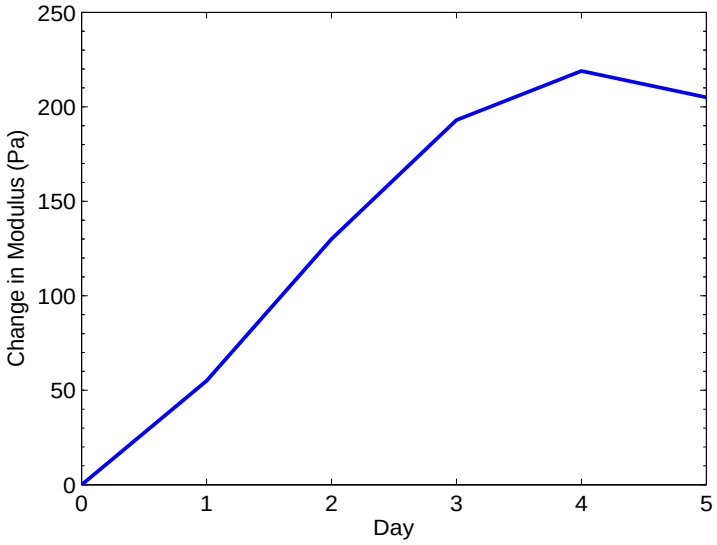

Figure 3.14: Change in Modulus with Growth of Cells

The stiffening effect that fibroblasts have in the matrigel can be attributed to collagen production. In a study by Emonard et al., it was found that fibroblasts produce type I and type III collagen when cultured on matrigel. 40% of the collagen produced is incorporated into the matrigel support structure [12]. The collagen incorporation into the matrigel structure could play a large role in the stiffening of the matrix observed through the mechanical studies. Collagen is a protein with superior mechanical properties due to it's consistency of collagen fibrils composed of a staggered array of ultra-long tropocollagen molecules [5]. Collagen fibrils come together to form fibers; even greater hierarchal structures [5].

Chapter 4

Discussion

Through the use of cell density determination, MRSI, indentation experiments and optical coherence tomography combined on a single three-dimensional culture matrix, information was gained regarding fibroblast biochemical, structural and migratory behaviors in matrigel. The information gained from each modality ties together and each adds a piece to the larger story of how fibroblasts alter their environment in the matrigel.

Matrigel is a reconstituted extract of basement membrane proteins derived from the EHS mouse tumor. It contains laminin, type IV collagen, heparin sulfate proteoglycans, nidogen and entactin [25]. Fibroblasts are not usually in contact with basement membranes except during wound healing, in granulation tissue and as a result of some pathological conditions such as liver cirrhosis [12] and cancer [11]. However, it has been shown that fibroblasts easily attach to a reconstituted basement membrane and their proliferation and biosynthetic activities are modified in comparison to 2-D culture in a flask [12]. Matrigel serves as a nurturing environment for fibroblast natural activities and is ideal for development of a multi-modality approach to imaging cellular activities.

Fibroblast proliferative behavior was studied by determining cell density with increased culture time in the matrigel. A method of cell retrieval was used for counting cells. Slow growth initially suggests that the fibroblasts took 2 days to acclimate to the matrigel before beginning to proliferate. The cells take time to recover after being trypsinized and removed from their original 2-D culture in the T-75 flask. Trypsin is poisonous to cells, so the acclimation period may be directly related to the degree of which the cells were exposed, which was approximately 5 minutes in all sample preparations. Although this acclimation period could have occurred, the data was fit well with an exponential growth curve ($r^2 = 0.983$). It is possible that the cell number was too low initially to show proliferative and metabolic changes, which were evident after 2 days of culture.

Fibroblast proliferation could also have been studied using confocal microscopy. GFP-vinculin labelled fibroblasts fluoresce in the images. Image slices taken through the depth of the gel can be used to estimate cell number in the volume. Confocal microscopy was not used because the GFP labelled fibroblasts did

not proliferate in a 2D culture flask at the same rate as un-labelled fibroblasts. The doubling rate for GFP labelled fibroblasts was approximately twice that of the un-labelled. This lower rate of proliferation could be due to the age of the cells, which was unknown. Cells of a high passage number could have lower proliferation rates than those of a low passage number. The un-labelled fibroblasts used for the project were of low passage (between passages 2 and 8) and they proliferated very rapidly in 2D culture (approximately 18-24 hour doubling time). Also, the lower proliferation rate of the GFP-vinculin labelled cells could be due to a harsh transfection procedure required for labelling. It was decided that the labelled and un-labelled fibroblasts were not behaving equivalently. Therefore, the GFP-vinculin fibroblasts were not used in studies. Confocal microscopy requires the fluorescent label for visualization, so the imaging was not used for cell density determination in the matrigel.

Migratory behaviors of fibroblasts inside matrigel were imaged using optical coherence tomography. Images showed that the fibroblasts moved toward the top and bottom surfaces of the gel as culture time increased. Despite the nutrient supply in the medium on top of the gel, more cells travelled toward the bottom. It is plausible that this migratory behavior is in response to the tissue culture-treated membrane at the bottom of the Millipore cell culture inserts to which the matrigel was bonded. This membrane is specifically treated to promote adherence and proliferation. This movement provides evidence that medium is able to reach cells throughout the 7mm matrigel depth. The mechanism for fibroblasts movement through the gel is likely through the fibroblast production of MMPs that break down collagen and other matrix proteins. Fibroblasts produce MMPs in wound healing processes to assist with turnover of ECM proteins to restore new healthy tissue [32]

Biochemical changes in the matrigel as a result of fibroblast metabolism were indicated by pH changes and were detected using MRSI techniques. A 2 day acclimation period, similar to that seen in the proliferation study, was evident in the pH measurements. The pH only decreased 0.008 from day 1 to day 2, but decreased 0.04 from day 2 to day 3 and 0.17 from day 3 to day 4. The decrease in pH is indicative of cell metabolism, caused by lactate production , which is one of the main by-products of fibroblast metabolism of glucose and glycogen [28]. Glucose and glycogen are the main sugars provided to the fibroblasts in the media used in the study. Data showed cell metabolism increased after 2 days of culture. A change in pH of -0.22 was detected over 4 days time. Natural tissue pH in the body is 7.4. However, in the extracellular space of cancerous tumors, pH has been detected as low as 6.0 [14]. Using the MRSI technique, 16% of the pH change that occurs in tumors, was detected in 4 days.

Although it was seen through OCT images that there was a distribution of fibroblasts, more at the top and bottom surfaces of the gel, a similar distribution in pH was not evident. There was no spatially

localized decrease in pH, just an overall decrease with time. The spatial pH gradient that stabilized with time was due to media seepage into the gel that was equilibrating with the higher pH matrigel. The lack of a localized decrease in pH was due to diffusion of the fibroblasts' acidic products. Spectra for pH determination was taken once every 24 hours. In 1 day's time, the lactic acid produced by the cells had diffused evenly throughout the gel, producing a decrease in pH homogenously. In contrast, localized acidic environments are evident in cancerous tumors. Although diffusion of metabolism by-products takes place in natural tissue, perfusion of blood through the tissue also occurs. In healthy tissue surrounding a tumor, the perfusion of blood quickly clears acidic products. However, tumor cells over produce acid due to increased metabolism and perfusion of these tissues is insufficient to maintain a pH of 7.4. Therefore, local pH values within regions of the tumor can be decreased significantly below 7.4.

Measurements of matrigel pH over time was limited to four days in the MRSI study due to the gradual removal of imidazole over time as the medium was replaced. Throughout the MRSI study, it was evident that the relative size and visibility of the imidazole peaks in the spectrum, and in particular the left (C2-H) peak, was decreasing with culture time. On day 5 of the study of the control matrigel, the C2-H imidazole peak was not visible. A matrigel-fibroblast sample was tested after 6 days of culture with the same result. This phenomenon was investigated to determine whether the samples were losing imidazole over time. The medium on top of the matrigel was changed each day on all samples, including the control. On a day 4 control sample, the media that was removed (1 day old) was placed into an NMR tube and the chemical shift spectrum was obtained. The presence of imidazole was detected through the appearance of the two imidazole peaks in the spectrum. The spectrum is shown in Figure 4.1. It is evident that the shrinking and eventual disappearance of imidazole peaks over the 5-6 day time frame was due to the medium leaching imidazole out of the gel. The medium was removed each day, so this was a significant loss. For longer studies of pH using the imidazole indicator, prevention of this loss would be necessary.

The loss of imidazole through removal of the media is another indication that the media seeps into the pores of the matrigel. This confirms that the pH gradient, evident in both the control and matrigel containing fibroblasts, is a result of media seeping into the matrigel over time. There is more media at the top of the gel and less gets through to deeper depths. Therefore, the pH gradient goes from lower pH at the top to higher as depth increases. This gradient decreases with time as the media equilibrates with the matrigel pH. The size of the gradient in the vertical direction begins to plateau at 3 days.

The mechanical property change in matrigel caused by fibroblasts was investigated using indentation. The results showed there were two competing mechanisms happening with time in the matrigel-fibroblast samples. The first mechanism is the equilibration of matrigel with medium and the incubation environment.

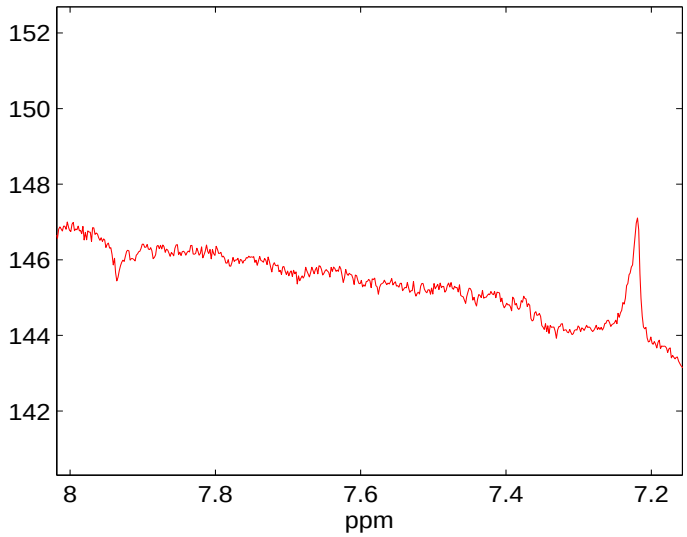

Figure 4.1: MRSI Spectrum Showing Imidazole Peaks in Media

This mechanism is evident through analysis of the control matrigel results. The data showed a decrease in elastic modulus over 2 days, which then stabilized. This is a the time it takes for the matrigel to equilibrate with the incubation temperature of 37°C and 5%CO_2 in air. This time period closely corresponds to the 3 days it took in the MRSI study for the size of the pH gradient to begin to level out. This indicates that the seepage of media into the top of the matrigel may also play a role in decreasing the modulus initially from day 0 to day 2.

The second mechanism occurring in the mechanical study of matrigel-fibroblast samples is increased elastic modulus due to fibroblast production of collagen. The elastic modulus data for the matrigel with fibroblasts shows that the cells were stiffening the matrigel over the 5 days of culture. The difference of control modulus and fibroblast modulus data shows that the matrigel was stiffened most over the first 3 days (55 Pa by day 1, another 75 Pa by day 2 and another 63 by day 3). After 3 days, the modulus increased 26 Pa by day 4 and showed a decrease by 14 Pa on day 5. This data shows that the modulus of the matrigel-fibroblast samples was beginning to plateau after 4 to 5 days. The stiffening of the matrigel caused by the fibroblasts overpowered the mechanism of equilibration with the incubation environment and media to produce overall increase in elastic modulus. The stiffening with time of the matrigel-fibroblast samples is due to fibroblasts' mechanism of collagen production and incorporation of the collagen into the matrigel.

Detection of the location of the fibroblasts in the gel, and therefore the location of their secretions of collagen, aids in better understanding specifics of how the modulus of the gel increased with culture time. OCT images showed the fibroblasts migrated primarily to the bottom of the matrigel. This would indicate

that the collagen deposition and stiffening effect would also happen at the bottom. Although the indentation test used for modulus determination only indented 1.5mm into the top of the gel, the mechanical properties of the bottom of the gel could still be detected. This can be compared to that of the boundary effects of the bottom of the container. As the bottom of the gel becomes stiffer, it is similar to a boundary becoming closer to the spherical indenter. The detection of the stiffness is due to the force field projection that spreads down and out in the gel with displacement of the spherical indenter. The force from the bottom, stiffer part of the gel in this field, can be felt by the indenter. Therefore, increased collagen at the bottom of the gel would increase the modulus measurement.

Histology was attempted in an effort to visualize and quantify collagen production by the fibroblasts in the matrigel. Matrigel-fibroblast samples used for mechanical study were frozen and cryosectioned. However, the cryosectioning was unsuccessful due to the nature of the matrigel material. The matrigel, which is gel at 37°C and liquid at 4°C, was melting as sections were cut. The resulting stained sections did not show a uniform matrigel material, but instead resulted in stringy clumps. An example of a section stained with hematoxylin and eosin and sirius red (for collagen) is shown in Figure 4.2.

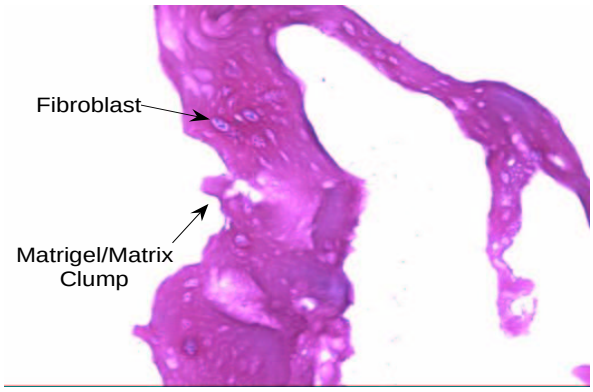

Figure 4.2: Histology of Matrigel-Fibroblast Section (40x Magnification)

Although cells and a fibrous matrix structure can be distinguished from the image, without a uniform section, distributions and relative quantization of collagen production was not possible. Had the sectioning of the matrigel been more successful, immunohistology could be done with an antibody that binds collagen I specifically for visualization. The matrigel contains collagen type IV, so a specific stain for collagen I is necessary to distinguish fibroblast collagen production from the matrigel. Also Hematoxylin and Eosin staining could show the distribution of cells in the gel to further validate the data from the OCT images.

Chapter 5

Summary and Future Work

Through this research, a multimodality approach to studying cellular level mechanisms of carcinogenesis was developed. A 3D matrigel structure was characterized and experimental setups were developed for use in imaging techniques. Spatial pH mapping of changes as a result of fibroblast metabolism were acquired through an MRSI technique utilizing an exogenous imidazole indicator. Mechanical changes with fibroblast culture were measured in the matrigel using a spherical indentation technique. Finally, migratory behavior was visualized through OCT imaging. The combination of these modalities provides spatial information regarding both structural and functional properties, on the molecular scale, of the matrigel-fibroblast cultures.

The multimodality approach developed can be used in future research to discover complicated molecular processes involved in tumor development. For examples, cancerous epithelial cells can be introduced into the gel to stimulate biologically relevant cell signalling, metabolic behaviors, and interactions with fibroblasts and the basement membrane matrix. Key mechanisms, metabolites, and structural characteristics discovered can be used to further develop the multimodality imaging into a diagnostic tool to improve clinicians' accuracy and spatial localization of disease states and abnormalities.

References

[1] G. A. Abrams, S. L. Goodman, P. F. Nealey, M. Franco, and C. J. Murphy. Nanoscale topography of the basement membrane underlying the corneal epithelium of the rhesus macaque. *Cell Tissue Res*, 299:39–46, 2000.

[2] J. Ackerman, G. Soto, W. Spees, Z. Zhu, and J. Evelhoch. The NMR chemical shift pH measurement revisited: Analysis of error and modeling of a pH dependent reference. *Magnetic Resonance in Medicine*, 36:674–683, 1996.

[3] V. M. Aleksandrov. Asymptotic solution of the contact problem for a thin elastic layer. *Prikl. Mat. Mekh.*, 33:61–73, 1969.

[4] J. Boussinesq. *Application des potentiels a léquilibre et du mouvement des solides elastiques*. Gauthier-Villars, Paris, 1885.

[5] M. Buehler. Nature designs tough collagen: Explaining the nanostructure of collagen fibrils. *Proceedings of the National Academy of Science*, 103:12285–12290, 2006.

[6] R. S. Chadwick. Axisymmetric indentation of a thin incompressible layer. *SIAM J. Appl. Math.*, 62:1520–1530, 2002.

[7] W. T. Chen and P. A. Engel. Impact and contact stress analysis in multilayer media. *Int. J. Solids Struct.*, 8:1257–1281, 1972.

[8] R. A. de Graaf and K. Nicolay. Adiabatic RF pulses: Applications to in vivo NMR. *Concepts Magn Reson*, 9:247–258, 1997.

[9] R. S. Dhaliwal and I. S. Rau. The axisymmetric Boussinesq problem for a thick elastic layer under a punch of arbitrary profile. *Int. J. Engr. Sci.*, 8:843–856, 1970.

[10] E. Dimitriadis, F. Horkay, and et al. Determination of Elastic Moduli of Thin Layers of Soft Material Using the Atomic Force Microscope. *Biophysical Journal*, 82:2798–2810, 2002.

[11] B. Elenbaas and R. Weinberg. Heterotypic Signaling between Epithelial Tumor Cells and Fibroblasts in Carcinoma Formation. *Experimental Cell Research*, 264:169–184, 2001.

[12] H. Emonard, J. A. Grimaud, B. Nusgens, Ch. M. Lapieŕe, and J. M. Foidart. End Products of Glucose and Glutamine Metabolism by Cultured Cell Lines. *J Cellular Physiology*, 135:151–155, 1988.

[13] J. Fujimoto, C. Pitris, S. Boppart, and M. Brezinski. Optical Coherence Tomography: An Emerging Technology for Biomedical Imaging and Optical Biopsy. *Neoplasia*, 2:9–25, 2000.

[14] M. Garcia-Martin, G. Martinez, and et al. High Resolution pH_e Imaging of Rat Glioma Using pH-Dependent Relaxivity. *Magnetic Resonance in Medicine*, 55:309–315, 2006.

[15] C. Gasparovic, I. Barba, J. Born, S. Barton, C. Arús, and P. Mann. A Study of Imidazole-Based Nuclear Magnetic Resonance Probes of Cellular pH. *Analytical Biochemistry*, 261:64–72, 1998.

[16] R. Gatenby, E. Gawlinski, A. Gmitro, B. Kaylor, and R. Gillies. Acid-Mediated Tumor Invasion: A Multidisciplinary Study. *Cancer Research*, 66:5216–5223, 2006.

[17] B. Gimi, A. Pathak, E. Ackerstaff, K. Glunde, and et al. Molecular Imaging of Cancer: Applications of Magnetic Resonance Methods. *Proceedings of the IEEE*, 93:784–799, 2005.

[18] J. Giron, R. Chisin, J.L. Paul, and et al. Multimodality imaging of cervical adenopathies. *European Journal of Radiology*, 21:159–166, 1996.

[19] W. C. Hayes, L. M. Keer, G. Herrmann, and L. F. Mockros. A methematical analysis for indentation tests of articular cartilage. *J. Biomech.*, 5:541–551, 1972.

[20] H. Hertz, U. die berunhrung, and E. Korper. On the Contact of Elastic Solids. *J. Reine Angew. Math*, 92:156–171, 1981.

[21] S. Van Huffel, R. de Beer, and D. van Ormondt. Advanced time-domain quantitation methods for MR spectroscopy and metabolite imaging. In *Proc. of the 18th Annual International Conference of the IEEE Engineering in Medicine and Biology Society*, Amsterdam, 1996.

[22] M. Insana, C. Barakat, M. Sridhar, and K. Lindfors. Viscoelastic Imaging of Breast Tumor Microenvironment with Ultrasound. *J of Mammary Gland Biology and Neoplasia*, 9:393–404, 2004.

[23] R. Kalluri and M. Zeisburg. Fibroblasts in Cancer. *Nature*, 6:392–401, 2006.

[24] J. B. Kim, R. Stein, and M. O'Hare. Three-dimensional in vitro tissue culture models of breast cancer - a review. *Breast Cancer Research and Treatment*, 85:281–291, 2004.

[25] H. Kleinman and G. Martin. Matrigel: Basement membrane matrix with biological activity. *Cancer Biology*, 15:378–386, 2005.

[26] W. Koźmiński and K. Jackowski. Application of adiabatic inversion pulses for elimination of baseline distortions in Fourier transform NMR. A natural abundance ^{17}O NMR spectrum for gaseous acetone. *Magn Reson Chem*, 38:459–462, 2000.

[27] K. Lang and M. Mueller et al. Regulation of cytosolic pH and lactic acid release in mesangial cells overexpressing GLUT1. *Kidney International*, 64:1338–1347, 2003.

[28] K. Lanks and P. Li. End Products of Glucose and Glutamine Metabolism by Cultured Cell Lines. *J Cellular Physiology*, 135:151–155, 1988.

[29] W. Luo, D. Marks, T. Ralston, and S. Boppart. Three-dimensional optical coherence tomography of the embryonic murine cardiovascular system. *Journal of Biomedical Optics*, 11:1–8, 2006.

[30] R. E. Mahaffy, C. K. Shih, F. C. MacKintosh, and J. Kas. Scanning probe-based frequency-dependent microrheology of polymer gels and biological cells. *Phys. Rev. Lett.*, 85:880–883, 2000.

[31] J. Makhoul. Linear Prediction: A Tutorial Review. *Proceedings of the IEEE*, 63:561–580, 1975.

[32] E. Olaso, J. Labrador, and et al. Discoidin Domain Receptor 2 Regulates Fibroblast Proliferation and Migration through the Extracellular Matrix in Association with Transcriptional Activation of Matrix Metalloproteinase-2. *The Journal of Biological Chemistry*, 277:3606–3613, 2002.

[33] G. I. Popov. The contact problem of the theory of elasticity for the case of a circular area of contact. *Pril. Mat. Mekh*, 26:152–164, 1962.

[34] D.L. Rabenstein and A.A. Isab. Determination of the Intracellular pH of Intact Erythrocytes by H-1-NMR Spectroscopy. *Analytical Biochemistry*, 121 (2):423–432, 1982.

[35] L. I. Sacolick, D. L. Rothman, and R. A. de Graaf. Adiabatic Refocusing Pulses for Volume Selection in Magnetic Resonance Spectroscopic Imaging. *Magn Reson Med*, 57:548–553, 2007.

[36] I. N. Sneddon. The relation between load and penetratoin in the axisymmetric Boussinesq problem for a punch of arbitrary profile. *Int. J. Engr. Sci.*, 3:47–57, 1965.

[37] W. Tan, A. Sendemir-Urkmez, and et al. Structural and Funcional Optical Imaging of Three-Dimensional Engineered Tissue Development. *Tissue Engineering*, 10:1747–1756, 2004.

[38] D. Townsend and S. Cherry. Combining anatomy and function: the path to true image fusion. *Eur. Radiol.*, 11:1968–1974, 2001.

[39] Y. O. Tu and D. C. Gazis. The contact problem of a plate pressed between two spheres. *Trans. ASME J. Appl. Mech.*, 31:659–666, 1964.

[40] A. van den Boogaart. Removal of the water resonance from ^{1}H Magnetic Resonance spectra. In J.G. McWhirter, editor, *Mathematics in Signal Processing III*, pages 175–195. Clarendon Press, Oxford, 1994.

[41] L. Vanhamme, T. Sundin, P. van Hecke, and S. van Huffel. MR spectroscopy quantitation: a review of time domain methods. *NMR in biomedicine*, 14(4):233–246, June 2001.

[42] Y. Yamamoto, Y. Nishiyama, and et al. Clinical Usefulness of Fusion of ^{131}I SPECT and CT Images in Patients with Differenctiated Thyroid Carcinoma. *Journal of Nuclear Medicine*, 44:1905–1910, 2003.

[43] F. Yang. Indentation of an incompressible elastic layer. *Mech. Mater*, 30:275–286, 1998.